CONTROLLED-SOURCE ELECTROMAGNETIC MODELING OF THE MASKING EFFECT OF MARINE GAS HYDRATE ON A DEEPER HYDROCARBON RESERVOIR

A Thesis

by

DAVID DICKINS

Submitted to the Office of Graduate Studies of
Texas A&M University
in partial fulfillment of the requirements for the degree of

MASTER OF SCIENCE

August 2007

Major Subject: Geophysics

CONTROLLED-SOURCE ELECTROMAGNETIC MODELING OF THE MASKING EFFECT OF MARINE GAS HYDRATE ON A DEEPER HYDROCARBON RESERVOIR

A Thesis

by

DAVID DICKINS

Submitted to the Office of Graduate Studies of
Texas A&M University
in partial fulfillment of the requirements for the degree of

MASTER OF SCIENCE

Approved by:

Chair of Committee, Mark Everett
Committee Members, John Hopper
Walter Ayers
Head of Department, John Spang

August 2007

Major Subject: Geophysics

ABSTRACT

Controlled-Source Electromagnetic Modeling of the Masking Effect of Marine Gas Hydrate on a Deeper Hydrocarbon Reservoir.

(August 2007)

David Dickins, B.S., The University of Texas at Austin

Chair of Advisory Committee: Dr. Mark Everett

The ability of marine controlled-source electromagnetic (MCSEM) methods to help image electrical conductivity contrasts below the Earth's surface makes them useful for both initial reconnaissance surveying for hydrocarbons and for delineating prospective regions of high resistivity in development drilling.

A 3-D finite-element MCSEM Fortran algorithm used for forward modeling was developed by Badea. Additional code was written and used for this thesis, with the goal of enforcing more realistic electromagnetic (EM) Dirichlet boundary value conditions.

The results of the new boundary conditions on a MCSEM survey model, with a hydrocarbon-saturated region in the subsurface, show that the method does not work as hoped. Constant boundary values were applied to gauge the transmitter-receiver (TX-RX) range at which results are not boundary influenced, using a hydrate/hydrocarbon model of the subsurface, at each of the three transmitter frequencies used in this study (1 Hz, 3 Hz, and 10 Hz). Results showed that electric field data were reliable to roughly 5000 m of TX-RX offset for the 1 Hz and 3 Hz cases, and to 6500 m offset for 10 Hz.

The gas hydrate/hydrocarbon model was then run with zero-value boundary conditions. The goal was to determine what effect changing parameters of the gas hydrate, including hydrate radius, thickness, and depth, have on the EXEXS (x-component of secondary electric field inline with the transmitter dipole axis) curves at various offset, particularly in relation to a hydrocarbon-only model of the subsurface response, so as to evaluate the EM masking effect the hydrate has on the hydrocarbon.

The results showed that the x-component of electric field in an inline survey is dominated by the hydrate response, in all cases studied, with a couple of exceptions. One exception is 1 Hz transmitter frequency at 2500 m to 3000 m offset when depth to top of the massive gas hydrate zone was greater or equal to 250 m. Receivers at these offsets would successfully detect the hydrocarbon target.

ACKNOWLEDGEMENTS

I would like to thank Dr. Mark Everett for his valuable time and guidance, as well as for the opportunity to work on such a fascinating and challenging topic in geophysics.

I also want to thank Alfonso Benavides, Ryan Lau, and Souvik Mukherjee, for several conversations regarding electromagnetics.

TABLE OF CONTENTS

Page

LIST OF FIGURES

FIGURE Page

1. INTRODUCTION

1.1 Previous Studies

Marine controlled-source electromagnetics (MCSEM) sounding is a geophysical prospecting method which can detect resistive (e.g. hydrocarbon-saturated) layers below the seafloor. Although the MCSEM method is currently being used by energy companies to prospect for hydrocarbons, its roots can be traced back to the early 1980s, at which time academic studies pioneered controlled-source techniques for the purpose of imaging young oceanic lithosphere (Chave and Cox, 1982).

To get a better perspective and understanding of MCSEM, I briefly examine the method of marine magnetotellurics (MMT), which is closely related to MCSEM. I then review some publications concerned with modeling seafloor hydrocarbon prospecting using MCSEM (in particular those publications that pertain to the forward modeling algorithm used for this thesis research), as well as other literature sources which describe actual academic and industry surveys.

The MMT method utilizes the inherent time variations in the Earth's natural magnetic field and the subsurface electric currents that are consequently induced. The natural magnetic field is assumed to be of downward-propagating plane-wave form, originating from a horizontal sheet of currents in the ionosphere at ~100 km altitude. Seafloor ratios of electric field and magnetic field components at differing locations, as a function of source frequency, provide information about subsurface electrical conductivity variations with depth. Because high frequency signals are rapidly

---

This thesis follows the style of Geophysics.

attenuated by the overlying seawater, only the low frequency variations provide significant electric and magnetic field amplitudes on the seafloor. This preferential selection of low frequencies means that only deep targets can be probed.

MMT has been used for decades in deep water by academics to infer mantle conductivity (Filloux, 1983). More recently, MMT has been used to detect deep hydrocarbons and for base-of-salt mapping. These hydrocarbons, though deep, are significantly shallower than the mantle. Their detection has been made possible by instrumentation improvements, which have increased signal to noise ratio for high-frequency signals (allowing for shallower imaging). Hoversten et al. (2000) used the MMT method to successfully map the base of salt (which is difficult to image using seismology) in the Gulf of Mexico, at a location where there is sub-salt petroleum (the Gemini prospect, whose existence is verified by wells drilled) 2-5 km below mudline, in 1 km water depth.

MCSEM has a comparative advantage over the MMT method for shallow marine targets. Unlike MMT, which utilizes natural-source currents, MCSEM uses a finite-source of current. The transmitter, usually an alternating current horizontal electric dipole (HED), is effectively grounded in the seawater close to the seafloor, which means that higher frequencies are not attenuated by the entire water column. This allows higher resolution in the shallow subsurface. The disadvantage of MCSEM is that the dipolar source geometry has to be “unfolded” from the responses prior to interpretation.

1.1.1 Numerical Studies

Two of the pioneers in the area of MCSEM numerical modeling were Dr. Mark Everett and his PhD advisor at the University of Toronto, Dr. R.N. Edwards. Everett and Edwards (1993) provided a 2.5-D (3-D source and 2-D earth model) finite-element numerical solution for time-domain MCSEM. Early-time electromagnetic (EM) step-off responses of mid-ocean ridge structures were studied. Everett and Edwards (1993) determined that the in-line electric dipole-dipole survey configuration showed great promise for imaging beneath the seafloor. Unsworth et al. (1993) provided a 2.5-D finite-element numerical solution in the frequency domain for a 3-D current source over a 2-D structure. The code used a triangular mesh with an HED transmitter to solve for the secondary electromagnetic fields. The code was equally adaptable to land or marine environments, but performed more efficiently for marine environment simulations, because rapid attenuation of secondary fields in seawater allowed the mesh to be terminated very close to the seafloor, allowing for a mesh with fewer elements.

Sinha (1999) illustrated, through 1-D modeling, that higher resistivity layers within the subsurface yield higher field amplitudes, when coupling between source currents and subsurface currents is primarily inductive. Sinha (1999) also showed that in an inline survey (in which receivers are placed in the direction along the source dipole axis) both horizontal and vertical current loops contribute to field response. This means that current from the source will be both galvanically and inductively coupled to currents flowing in the subsurface.

Badea, Everett, Newman, and Biro (2001) developed and used a fully 3-D, finite-element algorithm to solve controlled-source electromagnetic (CSEM) wireline induction logging (uses a current loop source) problems in layers of differing conductivities. A modified version of this code, which allows for a seafloor HED source, was used in this thesis. The solution is based on a formulation of the governing Maxwell's (diffusion) equations in terms of Coulomb-gauged potentials.

As described in Badea et al. (2001), a 3-D cylindrical mesh is generated with local refinement capabilities. The geometrical flexibility afforded by the tetrahedral finite-element mesh allows for a variety of structures to be modeled and can therefore be used to model subsurface heterogeneities and irregular seafloor bathymetry. This is a significant advantage that the finite-element method holds over the finite-difference method (in which grid boundaries must be aligned with constant-coordinate surfaces). Favorable comparisons were made with this code against previously published EM induction codes (Badea et al., 2001).

Joshua King, a former MS student of Dr. Mark Everett, used an adapted version of the code described by Badea et al. (2001) for frequency-domain forward modeling of various resistive disk (model for hydrocarbon reservoir) structures with CSEM in a marine environment. This modeling was an effort to simulate a MCSEM survey that a petroleum exploration company might undertake (King, 2004). Instead of simulating induction logging, he modeled an HED transmitter source grounded in seawater close to the seafloor, arranged inline with an array of electric field receivers (also positioned on the seafloor). This CSEM acquisition geometry is similar to that of Eidesmo et al.

(2002). A laterally-extensive (diameter considerably larger than height) cylindrical disk and a geometrically more complicated anticlinal structure were used to simulate hydrocarbon reservoirs. King studied the x-component of electric field along the x-axis, known as the EXEX response, as a function of transmitter-receiver (TX-RX) offset for various disk models. King worked at low frequencies (.005-1.00 Hz) and ran various models, changing parameters such as disk depth, disk radius, transmitter frequency, and transmitter location.

King concluded that, at short transmitter-receiver offsets, the EM response of the disks behaves similar to that of an infinite disk, but with increasing TX-RX offset, double half-space behavior is observed (as if the disk were not present). This is expected since the skin-depth attenuation and geometrical spreading of secondary source fields both increase with increasing TX-RX offset. King also determined that the parameters which most significantly impact the total electric field at the receiver array are transmitter frequency and location.

Ryan Lau, another former MS student of Dr. Mark Everett, used similar techniques to King in modeling hydrocarbon reservoirs with MCSEM, also at low frequencies (0.005-1.00 Hz). Lau modified the Badea et al. (2001) code, allowing for differing TX-RX configurations (Figure 1). He compared the EXEX (x-component of electric field on receiver axis inline with transmitter axis) TX-RX configuration, with the EXEY (y-component of electric field on receiver axis inline with transmitter axis) configuration and found that the EXEY orientation, in the range 0.1-0.05 Hz, is best for

imaging the edges of the simulated hydrocarbon structure, provided the transmitter is placed sufficiently far from the center of the hydrocarbon structure.

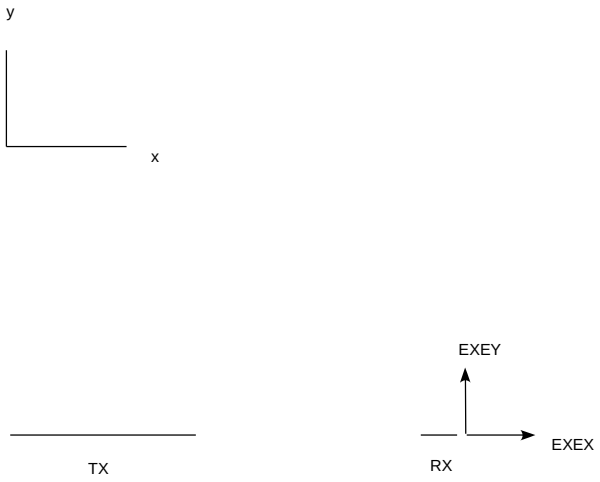

Figure 1. Plan view illustrating EXEX and EXEY configurations.

Constable and Weiss (2006) forward modeled and inverted the 1-D and 3-D responses of a thin hydrocarbon buried in the marine subsurface. Constable and Weiss (2006) determined that 1-D modeling, when source and receivers are over a hydrocarbon target, gives results which are very similar to the 3-D modeled response. They determined that this is because attenuation and geometrical decay provide for greatly decreased fields away from the TX-RX region, and therefore, lateral heterogeneity in this region yields relatively small field contributions.

1.1.2 Field Studies

Eidesmo et al. (2002) introduced a technique called Seabed Logging (SBL), which described and identified optimal survey designs for the direct imaging of deep marine hydrocarbon reservoirs using MCSEM. The SBL technique uses a near-seafloor mobile HED source (towed by a marine vessel via a shielded cable), with pre-deployed receivers spaced along the seafloor. The method takes advantage of the large contrast in conductivity between the sea-water saturated sediments and the hydrocarbon saturated reservoir.

Srnka et al. (2006) briefly outlined recent MCSEM surveys undertaken by ExxonMobil. Surveys were acquired in the Gulf of Mexico and offshore Scotland, West Africa, and South America. Some of the surveys were acquired simultaneously with drilling, production, and seismic acquisition. Srnka et al. noted that to satisfactorily determine the boundaries of the hydrocarbons, at the prospect scale, seismic data were needed in combination with CSEM survey results and modeling.

Moser et al. (2006) described a recent MCSEM survey by Shell that proved useful for imaging gas-saturated reservoirs in deepwater offshore Nigeria. Combining MCSEM data with seismic helped delineate the boundaries between those sands which were commercial targets for gas and those sands which were not commercially saturated with gas. This discrimination capability helps reduce the risk of drilling into non-commercial sands.

MacGregor et al. (2006) described a MCSEM survey performed over the Nuggets-1 producing gas field (operated by Total) in the North Sea. MacGregor et al.

(2006) showed that resolving subsurface resistive structures is significantly enhanced by inversion using structural information gained from seismic data as constraints. This successful application of MCSEM demonstrated that reservoirs can be accurately characterized in water depths much shallower (~115 m) than were previously thought to be practical.

1.2 Marine Controlled-Source Electromagnetics (MCSEM)

MCSEM can be particularly useful when used in conjunction with seismic surveys. Seismic waves are sensitive to acoustic impedance contrasts, but are not nearly as clear in differentiating between hydrocarbon saturated (higher resistivity) rock and seawater-saturated (lower resistivity) rock. Using MCSEM is also very useful in areas where the seismic data may be difficult to interpret due to scattering, such as areas with salt or volcanics.

A typical MCSEM survey consists of an alternating current horizontal electric dipole (HED) source, attached via a shielded cable to a ship. The source is typically towed a few tens of meters above the seafloor. A time-dependent current (with an associated primary electric field) is passed through the transmitter. When the primary field interacts with a medium of spatially variable conductivity (e.g. hydrocarbons, gas hydrates, salt, volcanics, etc…), a system of currents is induced. These induced currents have a secondary electric and magnetic field associated with them. The secondary EM fields diffuse through the sediments to be recorded by magnetic and electric field receivers spaced on the seafloor.

The attenuation of EM fields generated by a plane-wave source situated in a conductive wholespace is described by the skin-depth equation: $d_s = 503/\sqrt{\sigma f}$, where d_s is the skin depth (in m) of a medium with conductivity σ (in S/m) and frequency of transmitter f (in Hz). The skin depth is the distance over which the field attenuates by a factor of $1/e$.

Seawater has a conductivity which is typically higher than that of the sediments below the seafloor. The EM fields diffusing through the seawater attenuate rapidly and will be read only by receivers close to the transmitter. EM fields diffusing through the resistive marine subsurface, are attenuated by a lesser amount. The informative EM fields due to a resistive body in the subsurface (e.g. gas hydrates, hydrocarbon, or gas) will be poorly attenuated, such that measurable signals should be recorded at distant receiver offsets from the transmitter.

A common problem with MCSEM surveys in shallow-water is the air-wave effect (Figure 2). In shallow water, the EM signals diffuse up through the water column and come into contact with the air at the air-water boundary. Air has conductivity roughly eight orders of magnitude lower than seawater and does not attenuate the EM waves nearly as much as the seawater. These air-wave EM signals can diffuse laterally and then back down through the seawater to reach distant receivers along the seafloor. This “up-over-down” path is only an approximation, however, since the air and the seabed have a mutual inductance. Discriminating between the signals at the receivers due to the air-wave and those due to a resistive body in the subsurface can be very difficult. This is because an anomalously high electric field response due to the air-wave

may be similar to the response due to a buried hydrocarbon, depending on water depth and the structure of the resistor. An air-wave dominated electric field response is usually manifested by constant phase at large TX-RX offsets, because electric field has no phase loss in transit through the air. This is because the conductivity of air is very near zero, and conductivity causes phase changes.

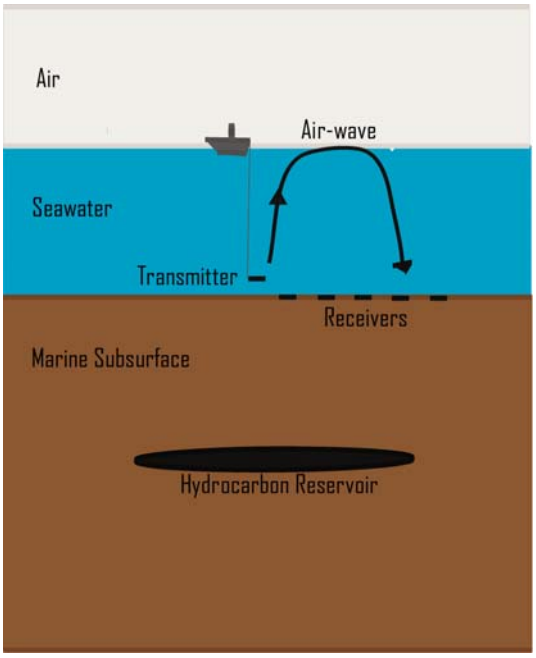

Figure 2. Conventional MCSEM survey, showing the air-wave effect. Idealized diffusion front (arrow path) is shown diffusing along the air/seawater interface and back down to receiver locations along the seafloor.

1.3 3-D Finite-Element Algorithm

The 3-D finite-element algorithm used for the research in this thesis was originally developed for interpreting global EM sounding data by Everett and Shultz (1996). Badea and Everett used an adapted version for interpreting borehole induction

logging data (Badea et al., 2001). The algorithm (now called *seatem*) has since been modified by Dr. Mark Everett of Texas A&M University for use in MCSEM modeling. The algorithm consists of routines devoted to mesh generation and routines devoted to solving the finite-element linear system. The mesh generator is capable of local refinement. Its basic structure is that of a quasi-uniform tetrahedralization of a cylindrical-shaped mesh of interconnected nodes (Badea et al., 2001). The matrix-solver part of the algorithm then solves Maxwell's diffusion equations in the Coulomb gauge for conductive medium. The user can select which regions of the mesh represent distinct geological units (such as hydrocarbon reservoirs), seawater, air, etc. The conductivity of these units and the receiver locations are also selected by the user.

Badea et al. (2001) developed a finite-element formulation in terms of gauged and coupled vector-scalar potentials ($\mathbf{A}, \Psi$), where $\mathbf{A}$ is the magnetic vector potential and Ψ is the electric scalar potential.

This formulation was selected to satisfy several conditions:

i) the normal component of electric field is allowed to jump across conductivity contrasts;

ii) the tangential component of electric field remains continuous across conductivity contrasts; and

iii) the EM potentials and fields contain no purely divergent spurious modes.

Primary potentials and fields are those arising due to the background model. Secondary potentials and fields are those arising due to anomalous resistivity structures within the subsurface (e.g. hydrocarbons and gas hydrates).

Once the finite-element matrix is solved and values of the secondary potentials are calculated at each of the (~100,000) node points, a moving least-squares interpolant (MLSI) differentiation method recovers the physically significant values of secondary magnetic and electric field values at the node points (Badea et al., 2001).

In the research undertaken for this thesis, only 'low' frequency responses ($w\varepsilon << \sigma$) are studied, where w is angular frequency, ε is electric permittivity, and $\sigma(\mathbf{r})$ is the spatially-variable conductivity of the medium. At these 'low' frequencies, displacement current density $\mathbf{J_D} = \frac{\partial \mathbf{D}}{\partial t}$ is negligible, compared to ohmic conduction current density $\mathbf{J_O} = \sigma\mathbf{E}$; that is, $\frac{\partial \mathbf{D}}{\partial t} << \sigma\mathbf{E}$.

A simplified derivation of the mathematical formulation found in Badea et al. (2001) begins with Amperes law, $\nabla \times \mathbf{H} = \frac{\partial \mathbf{D}}{\partial t} + \mathbf{J}$, where **H** is the magnetic field, **D** is the electric flux density (related to electric field **E**, by $\mathbf{D} = \varepsilon\mathbf{E}$), and **J** is the electric current density. In the low-frequency approximation, Ampere's law is reduced to $\nabla \times \mathbf{H} = \mathbf{J}$. Since **J** is composed of a source component $\mathbf{J_S}$ and an ohmic conduction component $\sigma\mathbf{E}$, we have

$$\nabla \times \mathbf{H} = \mathbf{J} = \mathbf{J_S} + \sigma\mathbf{E}. \qquad (1)$$

The second Maxwell equation is Faraday's law, $\nabla \times \mathbf{E} = -\frac{\partial \mathbf{B}}{\partial t}$, where **B** is magnetic induction, which in the frequency domain with e^{-iwt} time-dependence becomes:

$$\nabla \times \mathbf{E} = iw\mu_0 \mathbf{H}, \tag{2}$$

where we have set $\mathbf{B} = \mu_0 \mathbf{H}$, with μ_0 the magnetic permeability of free space. Equations (1) and (2), when combined, are known as Maxwell's diffusion equations, or separately they are called the pre-Maxwell equations (since Maxwell's main contribution was identification of the displacement current).

Badea et al. (2001) ensured the finite-element formulation conformed to $\nabla \cdot \mathbf{J} = 0$ (applies to 'low' frequencies) and $\nabla \cdot \mathbf{B} = 0$ (one of Maxwell's fundamental equations), which means no point sources or sinks of electric current or magnetic induction exist, outside the grounding points of the dipole transmitter. Additionally, the magnetic induction and electric field were expressed in terms of the magnetic vector potential **A,** and a reduced electric scalar potential Φ, as:

$$\mathbf{B} = \nabla \times \mathbf{A} \tag{3}$$

$$\mathbf{E} = iw\mathbf{A} - \nabla\Phi, \tag{4}$$

where the use of $\Phi = -iw\Psi$ leads to a symmetric finite-element matrix. Ψ is considered to be an "unreduced" potential, because its gradient does not equal electric field in the electrostatic case.

Badea et al. then rewrote (1) as

$$\nabla \times \nabla \times \mathbf{A} = \mu_0 \mathbf{J}_S + \mu_0 \sigma (iw\mathbf{A} - \nabla\Phi), \tag{5}$$

and used the formulation in terms of the Coulomb gauge ($\nabla \cdot \mathbf{A} = 0$) to add (without changing it) $-\nabla(\nabla \cdot \mathbf{A})$ to the left side of the equation, which yields

$$\nabla \times \nabla \times \mathbf{A} - \nabla(\nabla \cdot \mathbf{A}) - iw\mu_0\sigma(\mathbf{A} + \nabla\Psi) = \mu_0 \mathbf{J_S}. \qquad (6)$$

Since $\nabla \times \nabla \times \mathbf{A} - \nabla(\nabla \cdot \mathbf{A}) = -\nabla^2 \mathbf{A}$, a vector Helmholtz equation in the form

$$\nabla^2 \mathbf{A} + iw\mu_0\sigma(\mathbf{A} + \nabla\Psi) = -\mu_0 \mathbf{J_S}, \qquad (7)$$

emerges, with $\nabla \cdot \mathbf{J} = 0$ needed to solve the system of equations.

Badea et al. (2001) then wrote $\mathbf{A}$ and Ψ as the sum of primary potentials due to the source ($\mathbf{A}_p, \Psi_p$) in a known background structure $\sigma_p(z)$, and secondary potentials ($\mathbf{A}_s$, Ψ_s) arising due to the spatially varying conductivity distribution $\sigma_s = \sigma(z) - \sigma_p(z)$. The primary-secondary decomposition is $\mathbf{A} = \mathbf{A}_p + \mathbf{A}_s$ and $\Psi = \Psi_p + \Psi_s$. The homogeneous Dirichlet boundary condition ($\mathbf{A}_s$, Ψ_s) = ($\mathbf{0}$,0) is applied to the mesh boundary. The Dirichlet boundary condition is justified, because at the outer boundary of the mesh, the fields are far enough from the source that they are assumed to be negligible there (Badea et al., 2001). The system of linear equations that results from this formulation is solved by the quasi-minimal residual method (QMR) (Freund et al., 1992), which determines the potentials at all node locations within the mesh.

1.4 Motivation for Gas Hydrate/Hydrocarbon Study

Gas hydrates are structures composed of linked molecules of water (clathrates), which can act as trapping mechanisms for gas. A variety of different gases can potentially become trapped in these clathrate structures. Some of these gases include

methane, ethane, hydrogen sulfide, and carbon dioxide (Hardage and Roberts, 2006). Gas hydrates are stable only at low temperature range ($< 20^{\circ}$ C) and high pressure range (>30 atm), where water depth exceeds ~400 m. Gas hydrates are usually found in the first several hundreds of meters below the seafloor. Hydrates do not usually accumulate in the upper few tens of meters below the seafloor due to sulfate reduction: $CH_4 + SO_4 \rightarrow HCO_3 + HS + H_2O$ (Hardage and Roberts, 2006).

Free gas is often present below gas hydrate. The resulting layered structure can give rise to an acoustic impedance contrast that is large enough to generate a bottom-simulating reflector (BSR) on seismic data (Yorath et al., 1987). The BSR, when recognized in seismic sections is a direct indicator of the base of the gas hydrate zone. However, a BSR isn't always present (Hyndman and Davis, 1992), so that there may be no direct evidence of gas hydrates from seismic data alone.

Though gas hydrates can be considered a potential source of future energy, they are also potential drilling geohazards. Hydrates may stimulate shallow water flow (Hardage et al., 2006) which can severely impede drilling, result in lost time and money, and may cause a well to be abandoned (Hardage et al., 2006). Shallow water flow is the flow of water outside structural casing up to the seafloor (Hardage et al., 2006). Shallow water flow occurs in water depths greater than 500 m in the Gulf of Mexico, at shallow subsurface depths (Hardage et al., 2006). Another hydrate-related drilling hazard can occur in the form of a well blowout. This occurs if overpressured free gas below the gas hydrate is unexpectedly penetrated by the wellbore.

One indication of the presence of gas hydrates is high resistivity readings on well logs (Hato et al., 2006). The logged resistivity of massive gas hydrate can be as high as $100\,\Omega\,\mathrm{m}$ (.01 S/m) (Liu and Flemings, 2006). Gas hydrate is located in the shallow marine subsurface and can exhibit high resistivity contrasts relative to barren formations. In standard MCSEM inline surveys, gas hydrate accumulations could cause a large electric field response at receiver locations on the seafloor.

In this thesis, I address the possibility of an EM masking effect that gas hydrates could have on the responses from deeper hydrocarbon targets of exploration interest. Electric field receivers in conventional MCSEM surveys are sensitive to anomalously high resistivity structures within the subsurface. Thus, MCSEM data could record signals that are dominantly due to the energization of gas hydrate, even when a highly resistive hydrocarbon reservoir is present in the deeper subsurface.

The motivation for forward modeling in this thesis originates from the desire to determine whether electric field responses in a gas hydrate/hydrocarbon scenario are dominated by the shallower gas hydrate (Figure 3). The geometry of the gas hydrate structure is varied, whereas the structure of the hydrocarbon-bearing zone remains constant. The resulting EM responses will help in determining the effect that changing gas hydrate structure has on the relative EM masking of the hydrocarbon. Forward modeling the electric field responses that are due to hydrocarbon and those that are due to hydrocarbon and gas hydrate can potentially help those in industry with survey design (in regions where gas hydrate may be present). Additionally, forward modeling can be used as an initial step toward inversion of real data. Increased exploration risk when

prospecting for economic hydrocarbon targets may arise due to the EM masking that overlying gas hydrate may have on deeper conventional hydrocarbon reservoirs (in additional to drilling risks involved). Objectives for the modeling study portion of this thesis arise from the desire to understand this masking effect, and by doing so, reduce exploration and drilling risks associated with gas hydrates in hydrocarbon exploration.

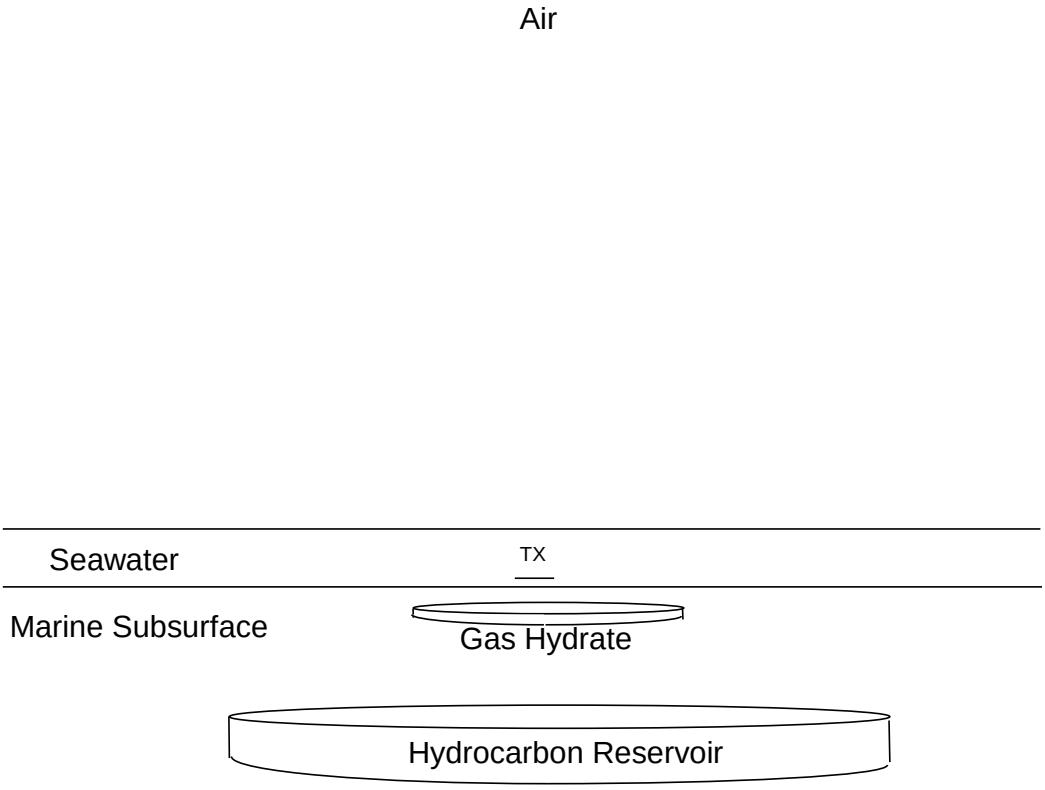

Figure 3. Cross section showing coaxial gas hydrate and hydrocarbon.

1.5 Objectives

The old zero-value Dirichlet boundary conditions can break down for shallow-water scenarios. New Dirichlet boundary conditions (EM potential values) are desired to

better characterize the EM potentials on the boundary (and thereby improve electric field characterization at receiver positions), for shallow water applications, such as those required for this study (500 m water depth). The Badea et al. (2001) code was modified to implement new Dirichlet-condition boundary values. The method uses the finite-element solution (for the EM potentials) on a larger, coarser-celled mesh as new boundary conditions on the boundary of a smaller, finer-celled mesh located within the former. Lelievre and Oldenburg (2006) originally suggested the basic method as a technique for improving magnetic forward-modeling studies.

The first objective is to determine whether the new boundary conditions allow for better electric field behavior at large TX-RX offsets. The geological scenario being modeled, for the gas hydrate/hydrocarbon masking study, as suggested by Dr. Johannes Singer of Shell, is a shallow-subsurface marine gas hydrate (drilling geohazard) located above a deeper hydrocarbon reservoir target, in 500 m water depth. Both the hydrate and the hydrocarbon reservoir are modeled as coaxial resistive cylindrical disks. Key parameters varied include hydrate radius, hydrate thickness, and hydrate depth.

The next objective of the study is to model a MCSEM survey that a hydrocarbon exploration company might undertake, in order to determine what effect changes in the gas hydrate may have on the total electric field response (due to responses of both gas hydrate and hydrocarbon target) at hypothetical receiver locations.

The final objective will be to determine to what extent the electric field responses at these receiver locations are dominated by gas hydrate, and therefore, whether the hydrocarbon (target) response is being masked.

2. METHODS

The MCSEM algorithm used for this research requires the conductivity model to be input. The primary, or background, model of the subsurface for the gas hydrate/hydrocarbon study is a three-layered earth. The top portion of the mesh represents air, the middle represents seawater, and the bottom portion of the background model represents the sea-water saturated marine subsurface. Each layer is internally homogeneous in terms of conductivity. Heterogeneity is introduced in the bottom layer, as it contains gas hydrate and hydrocarbon. The gas hydrate-saturated and hydrocarbon-saturated regions are each modeled as homogeneously conductive cylindrical disks (with coincident vertical axes) embedded within the shallow and deeper subsurface respectively.

The elements of the finite-element mesh conform to the cylindrical outer boundary of the solution domain. The mesh is constructed from tetrahedral elements, with each tetrahedron containing four nodes. Upon solution of the finite-element matrix and subsequent post-processing, each node contains electric and magnetic field values. Most important of these are nodes pre-selected by the user as receiver locations on the seafloor. The magnitude of the field values at these receiver locations can be plotted as a function of TX-RX offset to better understand how the EM response relates to the subsurface model. These field values as a function of TX-RX offset are among typical data recorded in MCSEM hydrocarbon prospecting surveys.

The mesh geometry is structured in terms of the cylindrical coordinates ρ, Φ, and z, but the potentials are solved in terms of their Cartesian coordinates

A_x, A_y, and A_z. The positive radial distance from the center of the mesh is ρ (in m), phi (Φ) is the azimuth (in rads), and z (positive downward) represents the distance in the vertical direction (in m). The top and bottom of the mesh are located at z=-1000 m and z=2000 m, respectively, and were chosen to encompass all the structures being modeled. Phi varies from $-\pi$ to $+\pi$, and the radius of the outer boundary (ρ_{max}) is 8000 m. The air region ranges from z=-1000 to z=-500, and is assigned a conductivity of $1 \cdot 10^{-8}$ S/m, as air is an effective insulator. The seawater interval ranges from z=-500 to z=0, and is assigned a constant conductivity of 3.2 S/m (neglecting temperature variations). The subsurface ranges from z=0 to z=2000, and the background sediments are assigned a uniform conductivity of 1.0 S/m. The conductivities used for this model were originally suggested by Steve Constable of Scripps Institute of Oceanography, and later used by King (2004) and Lau (2006).

The transmitter (TX) is an alternating current, horizontal electric dipole, with axis orientation inline with the string of receivers. The transmitter, the location of which can be varied, is located at x=0, y=0, and z=0, in Cartesian coordinates. The transmitter frequencies used in this study are 1 Hz, 3 Hz, and 10 Hz. These frequencies fall within the conventional frequency range for petroleum-based MCSEM surveys (Constable and Srnka, 2007). The receivers are linearly spaced every 250 m (along x-axis in Cartesian coordinates) on the seafloor (z=0). This inline EXEX (x-component of electric field on the x-axis) TX-RX configuration is a popular one that has been well-studied by oil companies (Srnka, et al., 2006) for both 3-D forward-modeling and interpretation of data from actual MCSEM surveys.

Localized third-order mesh refinement in the vicinity of the transmitter is utilized for the gas hydrate/hydrocarbon studies. Each level of refinement allows for improved spatial characterization of fields by a factor of two in any given coordinate axes direction. New nodes and tetrahedron are created in this region, which help improve characterization of the primary fields due to the transmitter. Improvement of the transmitter-generated primary fields in this critical region makes for more accurate secondary field characterization, because secondary current generation is dependent on the spatially varying characterization of the current source and its associated conduction-based primary electric field.

The hydrocarbon-saturated layer is modeled as a cylindrical disk, with uniform conductivity of 0.01 S/m. The disk has radius of 4000 m, thickness of 400 m, and is located at 1200 m below the seafloor, from z=1200 to z=1600, centered at x=0 and y=0.

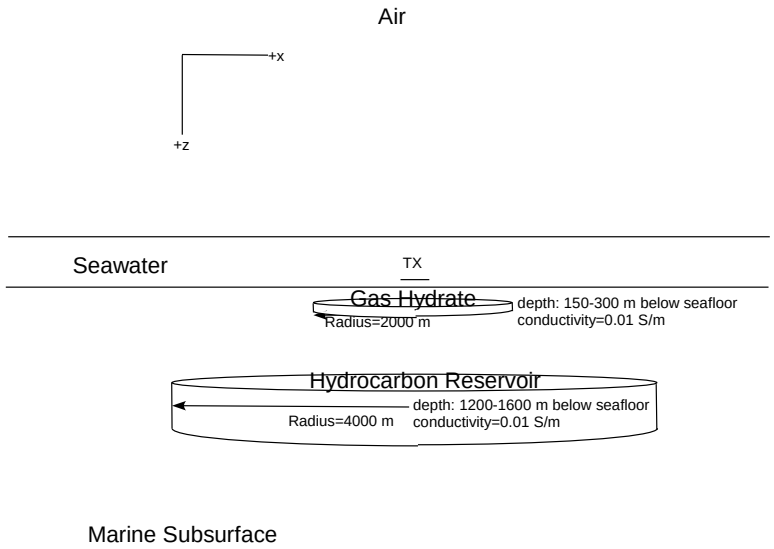

Figure 4. Default model of gas hydrate overlying hydrocarbon.

These hydrocarbon disk parameters will remain constant for the gas hydrate/hydrocarbon study (Figure 4).

The massive gas hydrate saturated layer is also modeled as a cylindrical disk, with default conductivity of 0.01 S/m. The default radius is 2000 m, default thickness is 150 m, and default location of the top of the hydrate is 150 m below the seafloor, centered at x=0 and y=0. The three main parameters of the gas hydrate which are studied include hydrate radius, hydrate thickness, and depth to the top of hydrate.

To study effect on EXEX response of hydrate radius, the values used for this parameter include: 250 m, 500 m, 1000 m, 2000 m, 4000 m, and 5000 m. For the hydrate thickness study, all parameters will be held constant, except for thickness. Gas hydrate thicknesses used include: 50 m, 100 m, 150 m, 200 m, and 250 m. For the hydrate depth study, all parameters are held to default values, except for the depth to the top of hydrate. Depths to the top of the gas hydrate saturated region include: 50 m, 100 m, 150 m, 200 m, 250 m, and 300 m.

The results are displayed as the logarithmic EXEXS (x-component of inline secondary electric field on x-axis) response as a function of linear TX-RX offset. Two main response curves are shown; that of the hydrocarbon-only model of the subsurface, and that of the model consisting of the shallower hydrate overlying the hydrocarbon target. For each of the end-member (minimum and maximum value of parameter being studied) hydrate/hydrocarbon curves, additional curves are displayed, which show hydrate/hydrocarbon response curves due to varying conductivity of the hydrate. In these end-member cases (250 m and 5000 m for radius, 50 m and 250 m for thickness,

50 m and 300 m for depth) hydrate conductivity is varied from the default value of 0.01 S/m, to additional values of 0.02 S/m, 0.05 S/m, 0.2 S/m, and 0.5 S/m. Increasing the conductivity of the gas hydrate layer demonstrates the effect on the EXEXS response as the saturation of hydrate within the pore spaces is decreased.

3. RESULTS

3.1 Dirichlet Boundary Condition Study

The goal of the research described in this section is to improve the MCSEM algorithm for shallow water depth scenarios, such as that used for the gas hydrate/hydrocarbon modeling study. Modification of the code for the new Dirichlet boundary values required significant fortran coding additions, in the form of two new subroutines.

The skin depth (spatial distance of exponential attenuation of the EM fields) is inversely proportional to the square-root of TX frequency and medium conductivity. In a shallow water model, relatively less electric field attenuation occurs, because less seawater exists (which spatially attenuates fields faster due to its higher conductivity). Therefore, zero-value Dirichlet boundary conditions become less valid than in a deeper water model. This provides motivation for improved boundary conditions, because improved potential value characterization on the boundary results in improved receiver field characterization. The homogeneous boundary conditions (magnetic vector potential and electric scalar potential are equal to zero on boundary) established in the current version of *seatem* are an approximation, owing to the fact that EM fields and potentials at nodes on the boundary are nearly zero due to their large distance from the source. This zero-value approximation is increasingly valid with increasing source-boundary distance.

If the source-boundary distance is increased, the zero-value boundary conditions are pushed outward radially and vertically (i.e. a new mesh is created with double the

radius and height). On the boundary of the larger and coarser (i.e. lower node density) mesh, the potentials are forced to go to zero (Figure 5). The finite-element solver calculated the potentials at all locations in the larger mesh, including nodes at the prior location of the boundary of the smaller mesh. This procedure yields more realistic boundary values of magnetic vector potential and electric scalar potential for a second computation on the original fine-mesh. Due to the differences in the node density of the two meshes, calculated values are present for roughly every fourth node on the boundary of the fine-mesh. Interpolation methods were therefore required to assign new values to nodes on the boundary of the fine-mesh.

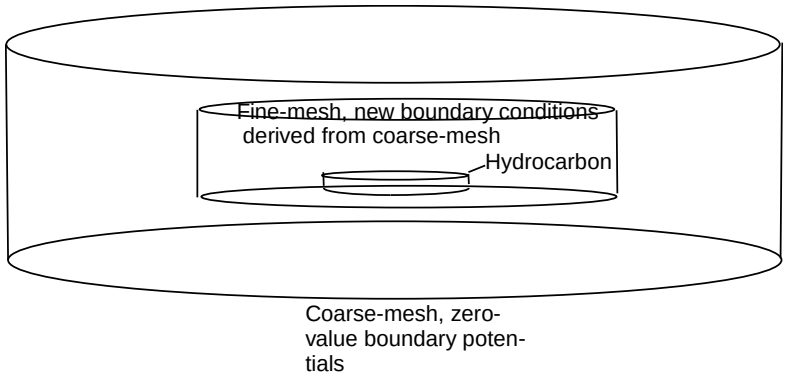

Figure 5. Fine-mesh and coarse-mesh for boundary condition study.

On the curved-wall boundary nodes of the cylindrical mesh, a cubic-polynomial interpolation is used. On the nodes on the top and bottom boundaries of the mesh, a 2-D "moving-least-squares interpolation" (Badea et al., 2001) is utilized. For the calculations on each of the meshes, three levels of local mesh refinement (so that the tetrahedra density in the vicinity of the transmitter is eight times greater than it otherwise

would be) are utilized in the vicinity of the transmitter. The total number of nodes and tetrahedra in each mesh scenario is held constant, which facilitates the use of the interpolation routines.

The interpolated potential values were compared to the original potentials, and the interpolation routines appear to be performing adequately, since plots of potentials (on the new fine mesh) as a function of z and phi show smoothly varying trends. Figure 6 shows that the secondary component of the electric scalar potential of the new fine-mesh conforms to the coarse-mesh derived boundary constraints at receiver locations near the fine-mesh boundary (8000 m). However the curve changes slope in an unexpected way, since psi for the new fine-mesh does not decrease steadily at offsets past 5000 m.

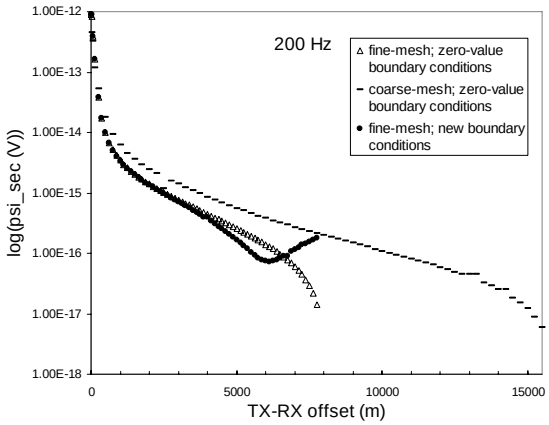

Figure 6. Secondary electric scalar potential (psi) as a function of offset at 200 Hz.

This procedure was tested at several different transmitter frequencies on a hydrocarbon-bearing model of the subsurface. The model of the subsurface included a hydrocarbon

saturated layer, with conductivity 0.01 S/m, at 1200 m to 1600 m below the seafloor, with radius of 4000 m, and an otherwise uniform subsurface (i.e. no gas hydrate layer in the overburden). It is important to note, that while transitioning from fine-mesh to coarse-mesh the size of the hydrocarbon and its depth do not change. A shallow water depth (50 m of water column) scenario is tested using the hydrocarbon model at relatively higher frequencies (200 Hz and 2000 Hz).

The 200-Hz EXEXS response at the receiver locations on the fine mesh with the new boundary conditions introduced a slight anomalous increase in EXEXS magnitude near the boundary. Maxwell's equations combined with the secondary horizontal electric dipole response due to the hydrocarbon disk, demand a steady decrease in EXEXS with increasing TX-RX range toward the boundary.

The new boundary conditions were then tested on the hydrocarbon model, in deeper water (500 m water column). Figure 7 shows the results of the new applied boundary conditions at 30 Hz, 100 Hz, and 200 Hz frequencies of the transmitter. In each case, the original fine-mesh with zero-value boundary conditions and the fine-mesh with new boundary conditions are identical in structure, with mesh height of 5000 m and mesh radius of 8000 m. The coarse mesh, from which the new boundary conditions were derived, has a height of 10,000 m and radius of 16,000 m. The receiver positions are spaced along the x-axis and on the seafloor (z=0).

If the method performed as hoped, we would expect to see all three curves coincide at the TX-RX offsets far from the boundary (near zero TX-RX offset), with slight curve separation between the fine-mesh zero-boundary and the coarse-mesh zero-

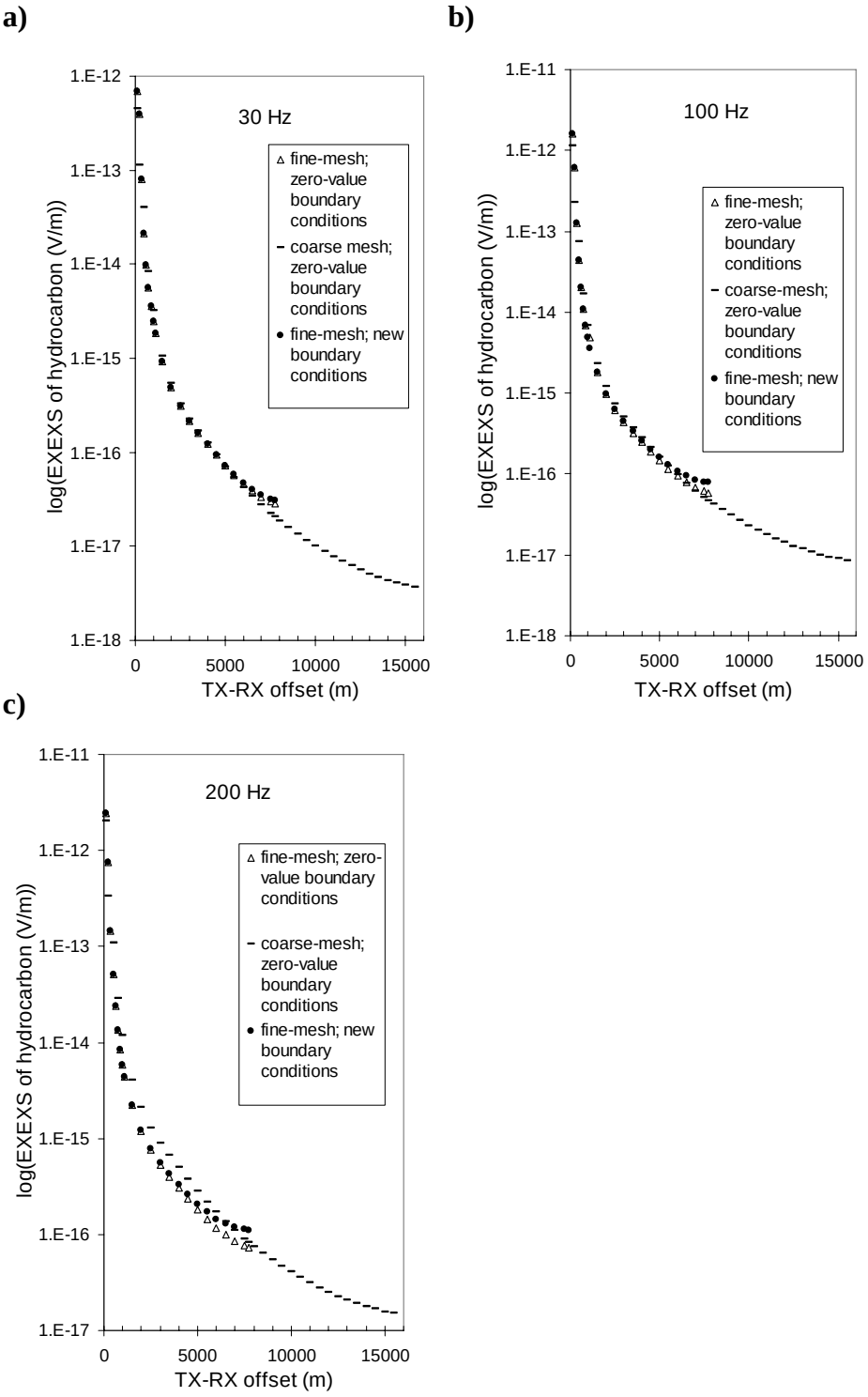

Figure 7. EXEXS response of hydrocarbon for boundary condition study. (a) 30 Hz, (b) 100 Hz, and (c) 200 Hz.

boundary curves with further increase in offset. With increasing TX-RX offset, the EXEXS response of the fine-mesh with new boundary conditions should begin to merge with the response of the coarse-mesh zero-boundary response and near the fine-mesh boundary (x=8000 m), the two curves should overly. The EXEXS responses of the fine-mesh with new boundary conditions on Figures 7a and b begin as expected at near to mid-range TX-RX offsets, but decrease in slope and diverge from the coarse-mesh zero-boundary response near the fine-mesh boundary. The EXEXS response of the fine-mesh with new boundary conditions as shown on Figure 7c (200 Hz) starts out as expected at very near offsets (up to about x=1000 m), but does not converge to the coarse-mesh zero-boundary response until around x=6500 m. From x=6500 m until x=7750 m the two curves diverge.

These responses show that the method clearly does not work as hoped. In Figures 7a and b the new-boundary EXEXS curve fails to converge with the coarse-mesh solution near the boundary. However it is important to note that in those two cases (30 Hz and 100 Hz), the coarse-mesh zero-boundary response is actually lower in magnitude than the fine-mesh zero-boundary response at offsets near the fine-mesh boundary (x=8000 m). This is unexpected, because at this location, the coarser mesh is further away from its zero-boundary condition and should therefore exhibit a larger magnitude response than the fine-mesh. In Figure 7c, the coarser mesh has a larger magnitude response (near the fine-mesh boundary) than the zero-boundary fine-mesh, as expected. However, the new-boundary fine-mesh response fails to consistently coincide

with the coarse-mesh zero-boundary EXEXS response at mid-range to long-range TX-RX fine-mesh offsets.

I suspect that the method failed to work, because the boundary conditions being applied to the new fine-mesh existed at several thousand node points. Having the solution conform to such a large number of different non-zero boundary values may have provided for slightly unstable solution convergence, even though the interpolation allowed for smooth variation of potentials.

This boundary condition method fails to improve the boundary conditions in shallow water scenarios. As a result, the remainder of the gas hydrate/hydrocarbon study is conducted at relatively lower frequencies (1 Hz-10 Hz). This frequency range is more typical of frequencies used by exploration companies conducting surveys in deepwater at present time. In the following section, a method will be used in which TX-RX offsets which are not boundary influenced will be determined for each of the three transmitter frequencies used for the gas hydrate/hydrocarbon research.

3.2 TX-RX Reliability Range Determinations

To obtain a rough estimate of the maximum TX-RX offset that the simulated EXEXS responses due to the default gas hydrate/hydrocarbon model are reliable, particularly near the mesh boundary, I examined the response as a function of TX-RX offset, using various constant positive boundary values for the potentials. Artificial boundary values were chosen to determine a “reliability zone” in which EXEXS responses are not affected by the outer boundary condition. Figures 8a-c shows the 1

a)

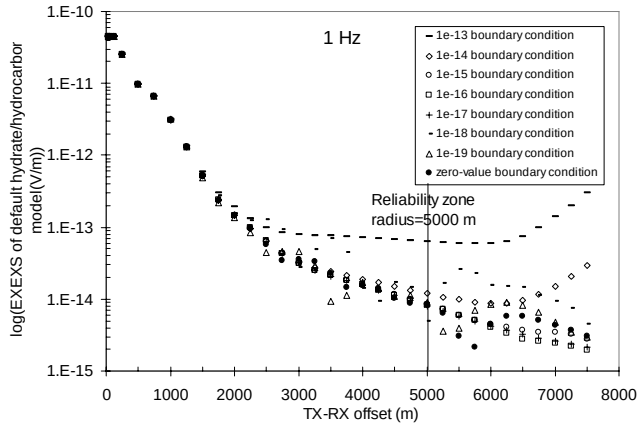

b)

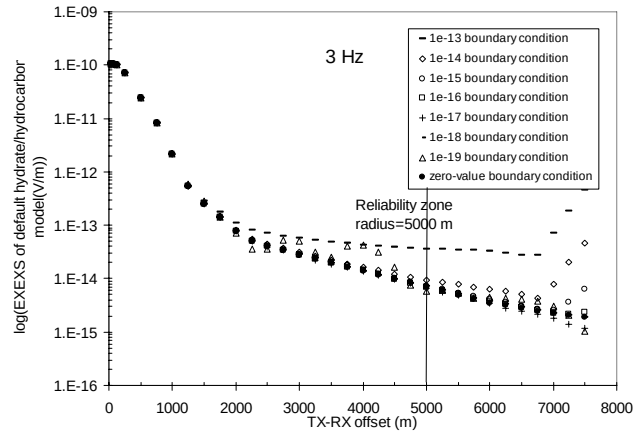

c)

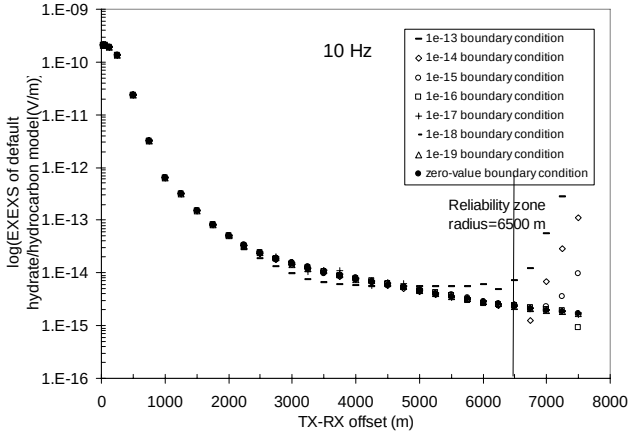

Figure 8. Reliability ranges. EXEXS response of gas hydrate/hydrocarbon model subjected to constant boundary conditions. (a) 1 Hz, (b) 3 Hz, and (c) 10 Hz.

Hz, 3 Hz, and 10 Hz EXEXS responses of the default model when subjected to various boundary conditions, ranging from $1e^{-13}$ (in Tm or V) to zero.

The maximum TX-RX offset at which responses provide reliable results, is called the radius of the reliability zone. The reliability radius is defined as the offset at which the EXEXS curves for artificially imposed boundary values start to (consistently) diverge. From Figures 8a-c, we see that the boundary condition of $1e^{-13}$ is unreasonably high, for the standard subsurface model. The other boundary conditions yield more plausible responses, in terms of characterizing the EXEXS responses due to the combination of the gas hydrate and hydrocarbon layers acting as secondary sources of electric field.

From Figures 8a and b (1 Hz and 3 Hz), the EXEXS responses begin to consistently diverge around a TX-RX offset of roughly 5000 m. Figure 8c (10 Hz) shows an EXEXS curve separation at around 6500 m offset. From this point on, graphs of EXEXS as a function of TX-RX offset, will only be shown up to a maximum offset of 5000 m, 5000 m, and 6500 m, for the 1 Hz, 3Hz, and 10 Hz frequencies of the transmitter, respectively. These values determine the radius of the reliability zone. Offsets greater than those mentioned are considered to be unreliably boundary-influenced. Zero-value homogeneous Dirichlet boundary conditions are henceforth applied everywhere on the mesh boundary for the parametric gas hydrate/hydrocarbon studies.

3.3 Hydrate Radius

In this section, I explore the effect of varying the hydrate radius on the EXEXS responses of the hydrate/hydrocarbon model. The goal here, and in the following two sections, is to gauge the degree to which responses at receiver locations are dominated by either the gas hydrate or the hydrocarbon. If addition of the gas hydrate to the hydrocarbon model of the subsurface increases the electric field by roughly an order of magnitude or more, the gas hydrate will be considered to be "masking" the hydrocarbon.

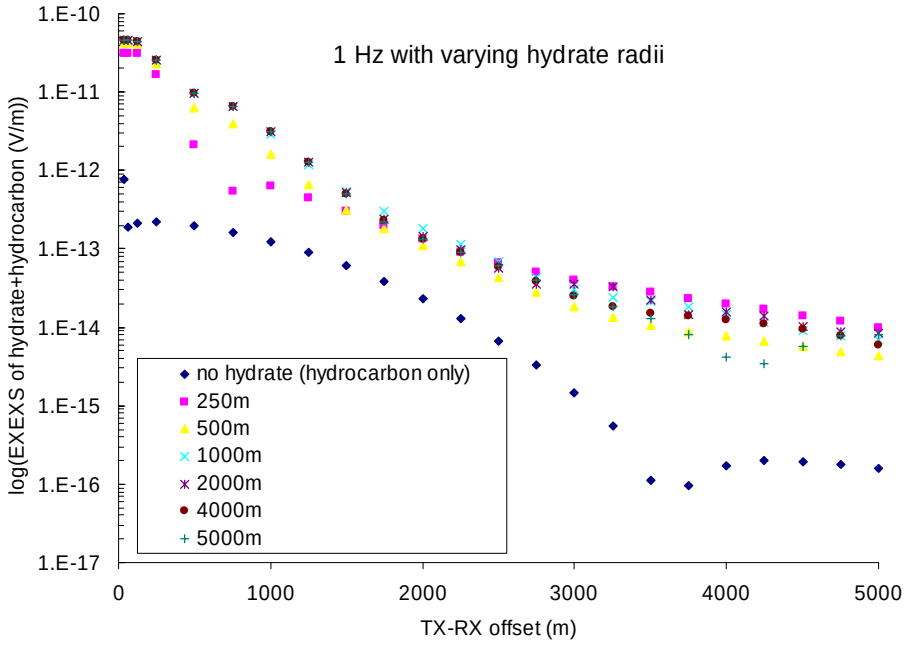

Figure 9. Varying hydrate radii. EXEXS response with varying hydrate radii (250 m-5000 m) in the hydrate/hydrocarbon model at 1 Hz.

Hydrate disk radii studied include: 250 m, 500 m, 1000 m, 2000 m (default), 4000 m, and 5000 m. I collectively refer to the maximum and minimum parameter values as the "end-members", and the values in between as "intermediate". In addition to varying the hydrate radius, I illustrate (on the end-member graphs) the effect on EXEXS responses as hydrate conductivity (denoted as sigma_hydrate on graphs) is varied. The different conductivities include: 0.01 S/m (default), 0.02 S/m, 0.05 S/m, 0.2 S/m, and 0.5 S/m. Increasing hydrate conductivity corresponds to decreasing hydrate saturation. The model of the subsurface in which zero gas hydrate saturation is included is denoted on the graphs as "no hydrate (hydrocarbon only)".

Figure 9 shows what happens at 1 Hz transmitter frequency as gas hydrate radii is varied. Larger hydrate radii results in a relatively larger EXEXS response up to ~2000 m offset. Past this offset the opposite trend is apparent.

Figure 11 shows the end-member modeled responses using the 250 m and 5000 m gas hydrate disk radii at 1 Hz transmitter frequency. The hydrocarbon-only response is identical in Figures 11a and b, since all the parameters of the hydrocarbon model including TX frequency are held constant.

The EXEXS response due to the hydrocarbon-only model shows a maximum at low TX-RX offsets, because secondary fields originating from the hydrocarbon bearing zone are greatest (Figure 10). At 3,500 m-3,750 m offset, a cusp of the EXEXS response is evident. This corresponds to locations on the receiver axis (x-axis) where the secondary electric field is predominantly vertical. At this location horizontal

contributions are minimal. The location of the cusp depends on the subsurface conductivity model. Normalized plots are not being utilized, because the cusp effect makes them difficult to interpret.

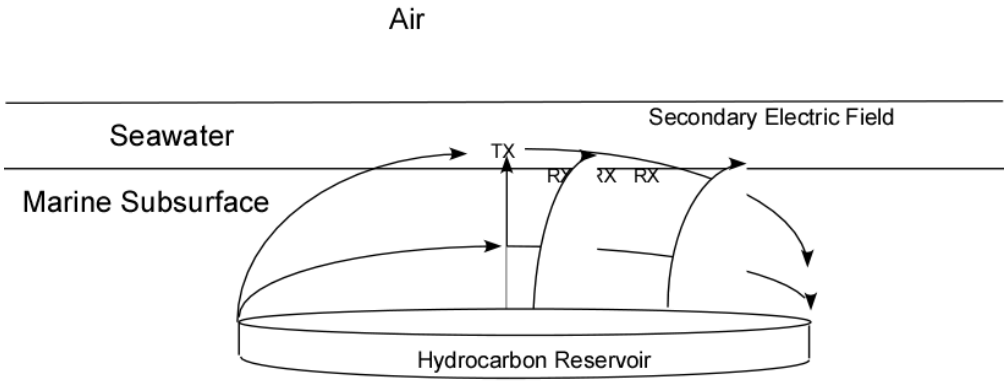

Figure 10. Secondary fields. Cross section showing idealized secondary electric field lines (arrows), in RX vicinity. The hydrocarbon acts as a secondary source of electric field.

Figures 11a and b show that as hydrate radius is increased from 250 m to 5000 m, relatively small changes in EXEXS occur. For the 250 m case, increasing the hydrate conductivity results in lower EXEXS responses. This is understood since the conductivity contrast between the hydrate and the surrounding sediments is reduced. This behavior is also apparent in the 5000 m case, except for the TX-RX range 2500 m-4500 m. In this range, the responses from higher hydrate saturations (with lower

a)

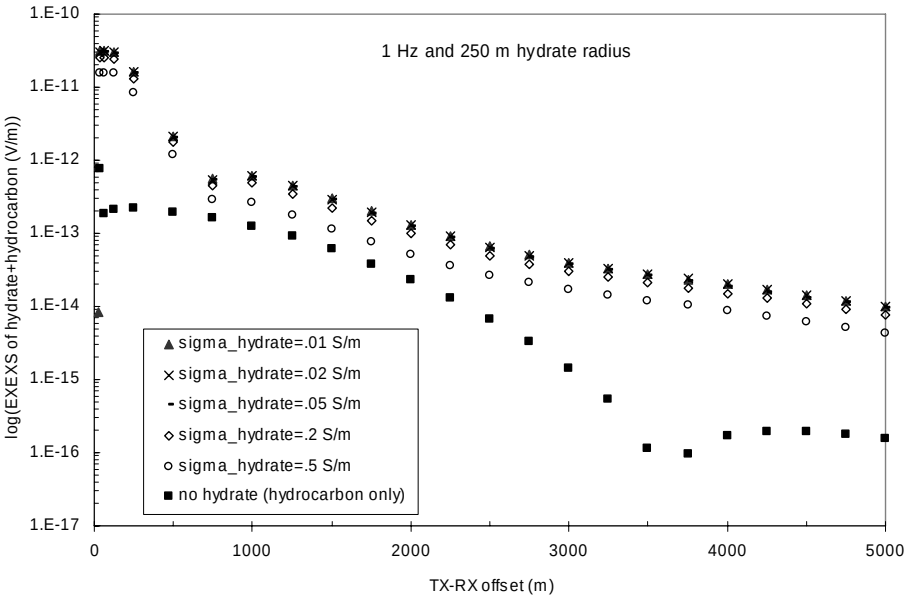

b)

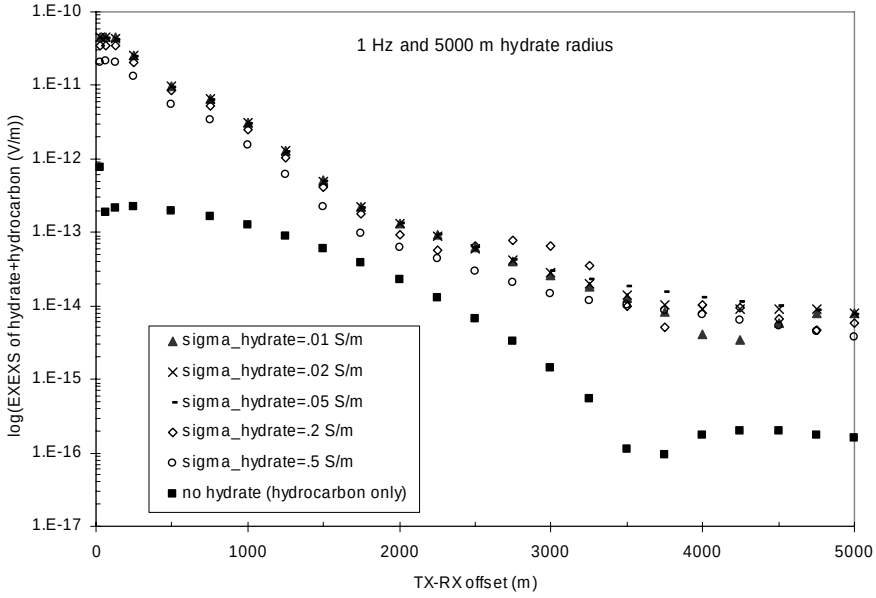

Figure 11. Gas hydrate/hydrocarbon 1 Hz endmember radii. (a) 250 m hydrate radius and (b) 5000 m hydrate radius.

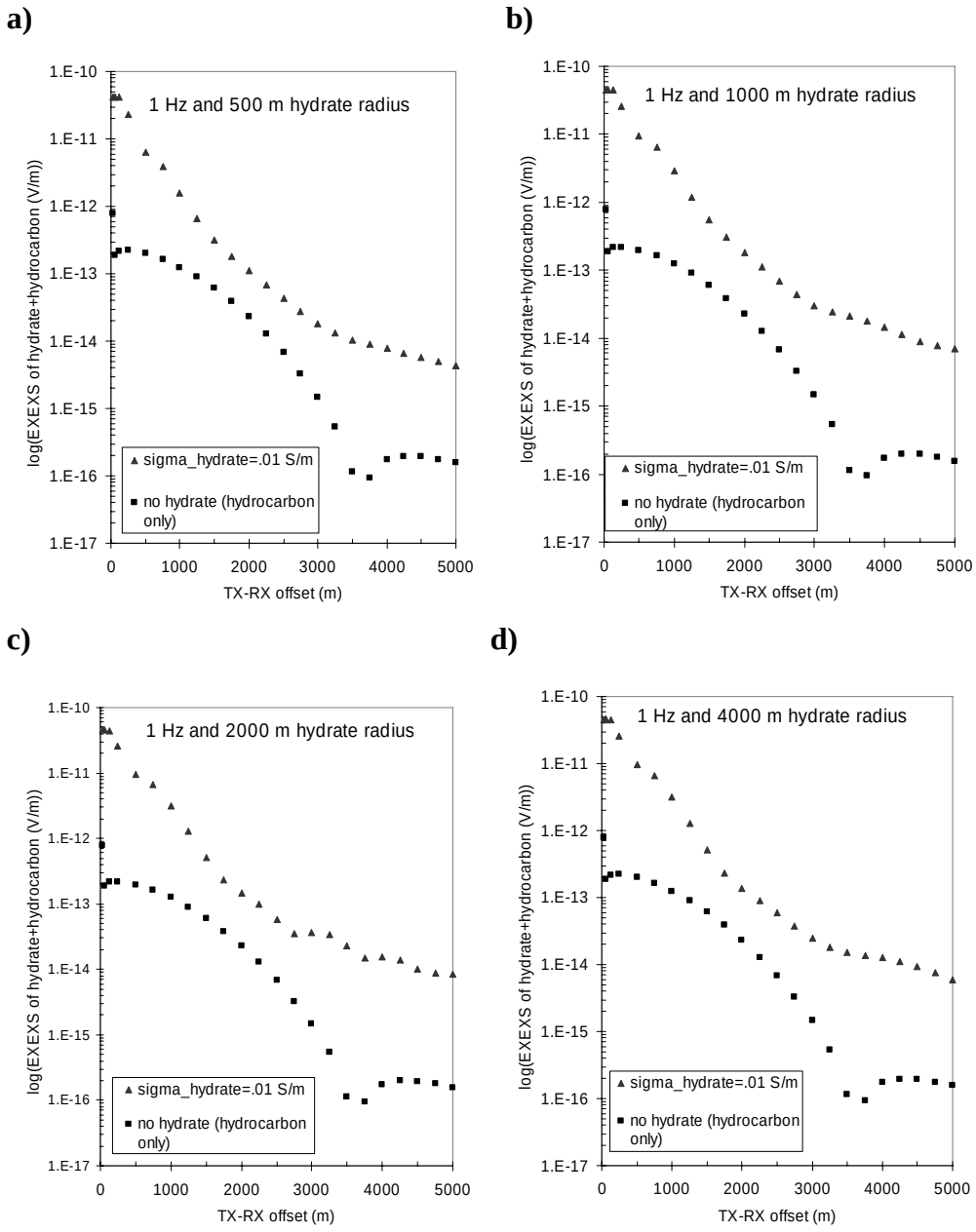

Figure 12. Gas hydrate/hydrocarbon 1 Hz intermediate radii. (a) 500 m, (b) 1000 m, (c) 2000 m, and (d) 4000 m.

conductivities) reach their respective cusps and fall below responses associated with the higher hydrate conductivities.

In Figures 12a-d, I show the intermediate radii results. From these graphs and from those of Figure 11, we notice that introducing hydrate with default conductivity into the subsurface results in a 1.0-2.5 order of magnitude increase in EXEXS regardless of the hydrate radius. Figures 11 and 12 show that minimum masking effect of hydrate on hydrocarbon occurs around 2000 m offset, as this is where the curves come closest together. Even here, introduction of the hydrate still results in an EXEXS perturbation about four times as large as the hydrocarbon-only response, meaning that receivers are primarily sensing EXEXS anomalies due to the hydrate. The conclusion is that at 1 Hz, the masking effect of the hydrate is very dramatic.

Figures 13a and b show the results at 3 Hz of the end-member radii. There is a relatively small percentage increase in magnitude of the horizontal component of secondary electric field at near offsets, when hydrate radius is enlarged from 250 m to 5000 m. At further offsets, increasing the radius from 250 m to 5000 m results in reduced EXEXS. This may be because fringing electric field (Figure 15), due to galvanic differential charge buildup on the top and bottom surfaces of the hydrate, has contributions which are largely horizontal in proximity to the hydrate edge.

a)

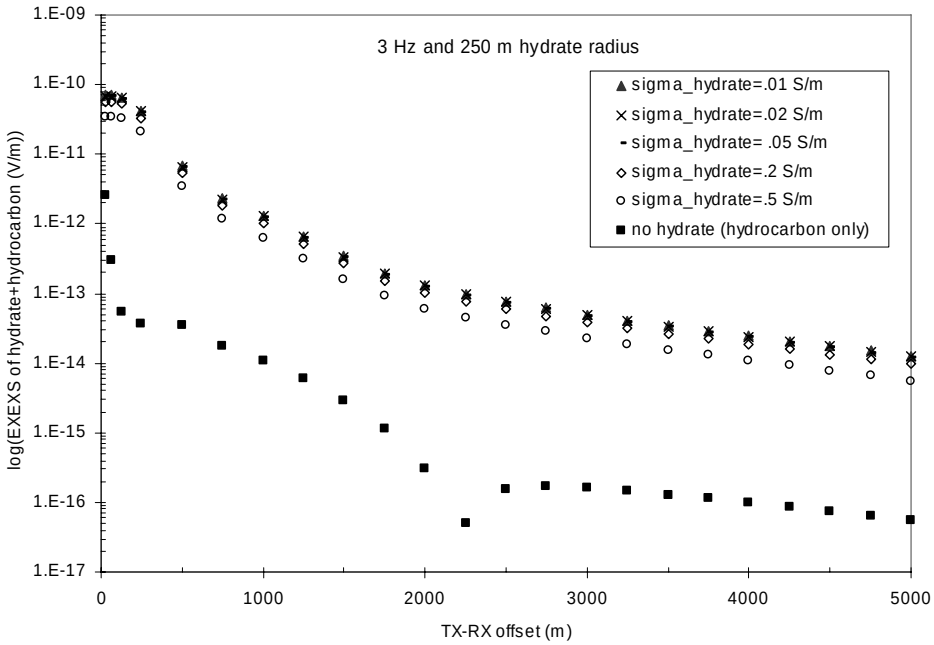

b)

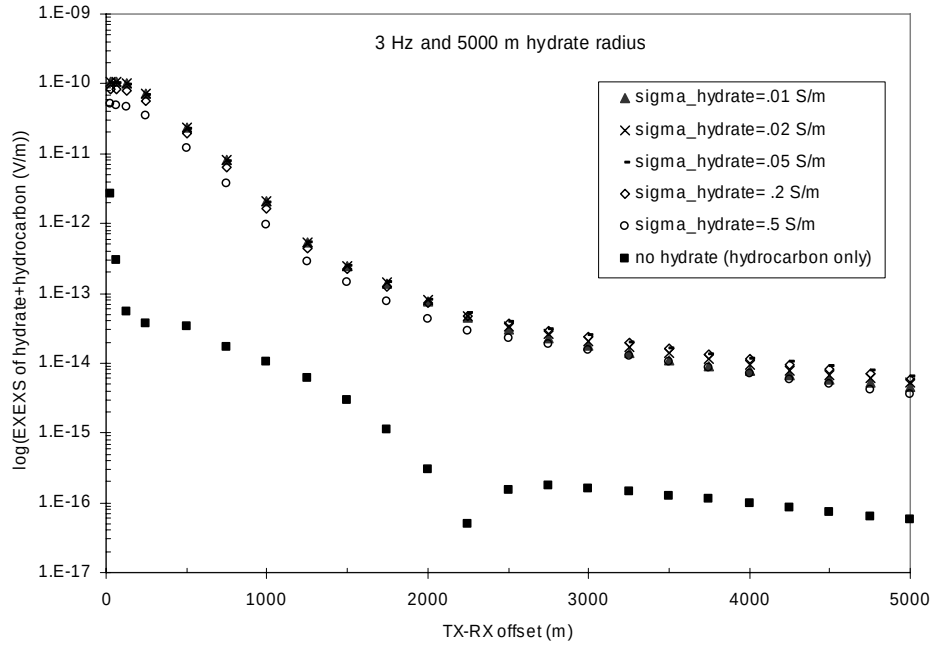

Figure 13. Gas hydrate/hydrocarbon 3 Hz endmember radii. (a) 250 m hydrate radius and (b) 5000 m hydrate radius.

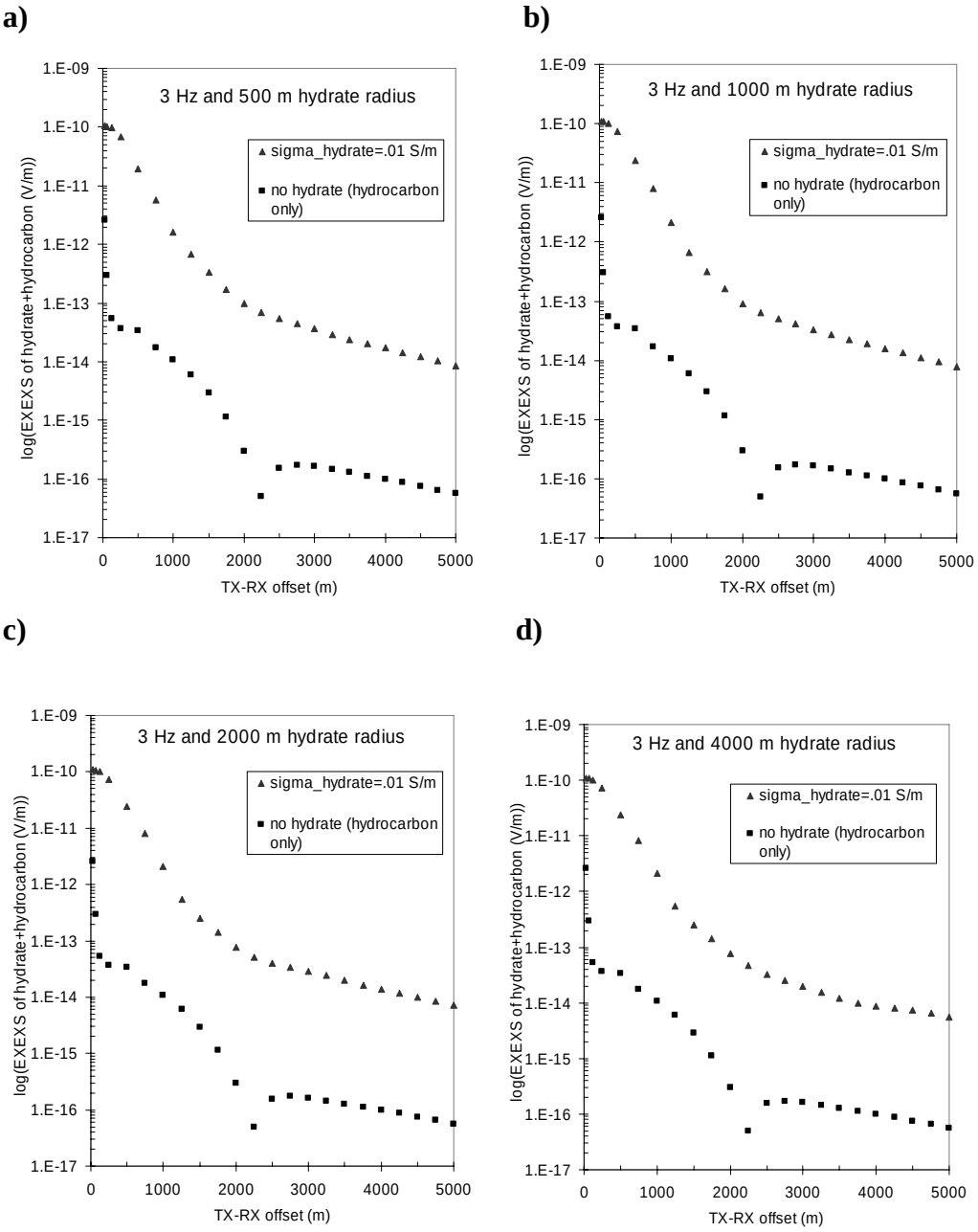

Figure 14. Gas hydrate/hydrocarbon 3 Hz intermediate radii. (a) 500 m, (b) 1000 m, (c) 2000 m, and (d) 4000 m.

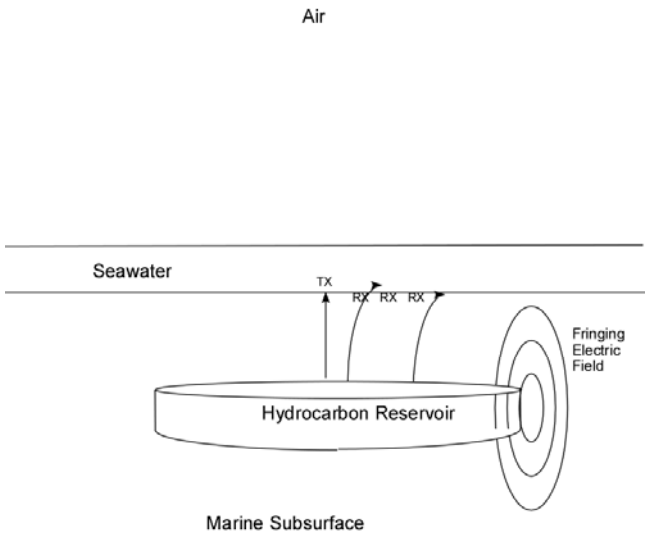

Figure 15. Fringing fields. Cross section showing idealized secondary fringing electric field diffusing from hydrocarbon edge.

Less decay in EXEXS may therefore result past 5000 m offset, for the 5000 m radius model. Offsets past 5000 m are not shown, because they are past the reliability radius for 3 Hz.

Figures 14a-d represents the 3 Hz intermediate radii model results. Curves exhibit a high degree of similarity, as the hydrate radius is increased. However, similar trends to those just stated are present, with increasing radius. From Figures 13 and 14, we may conclude that at 3 Hz, receiver responses at all offsets are dominated by the hydrate, regardless of radii.

Figures 16a and b show the 10 Hz hydrate radii end-member curves. From these and the intermediate radii curves in Figures 17a-d, I again conclude that the gas hydrate is masking the hydrocarbon response at all offsets, regardless of radius.

a)

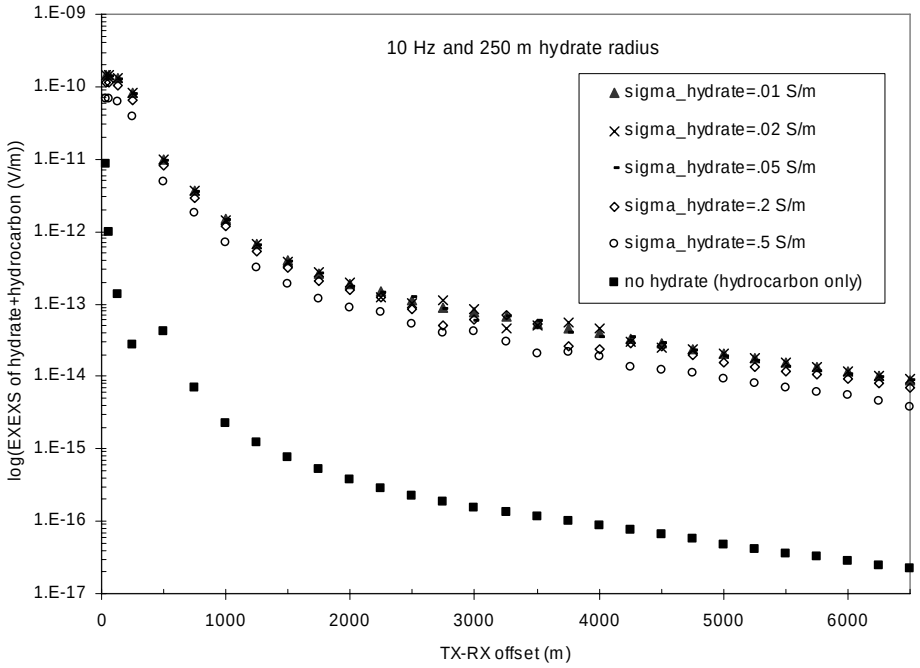

b)

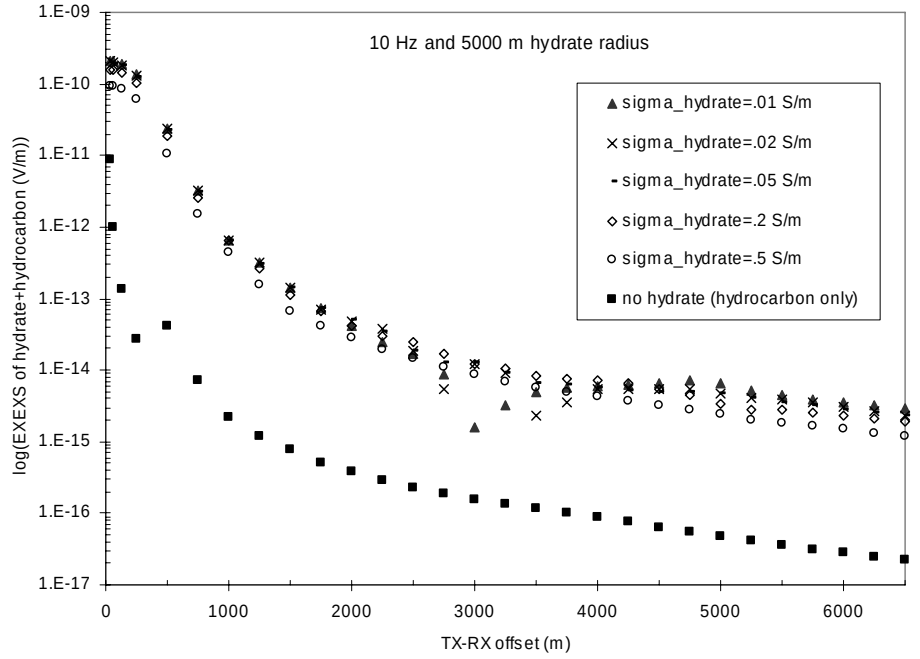

Figure 16. Gas hydrate/hydrocarbon 10 Hz endmember radii. (a) 250 m hydrate radius and (b) 5000 m hydrate radius.

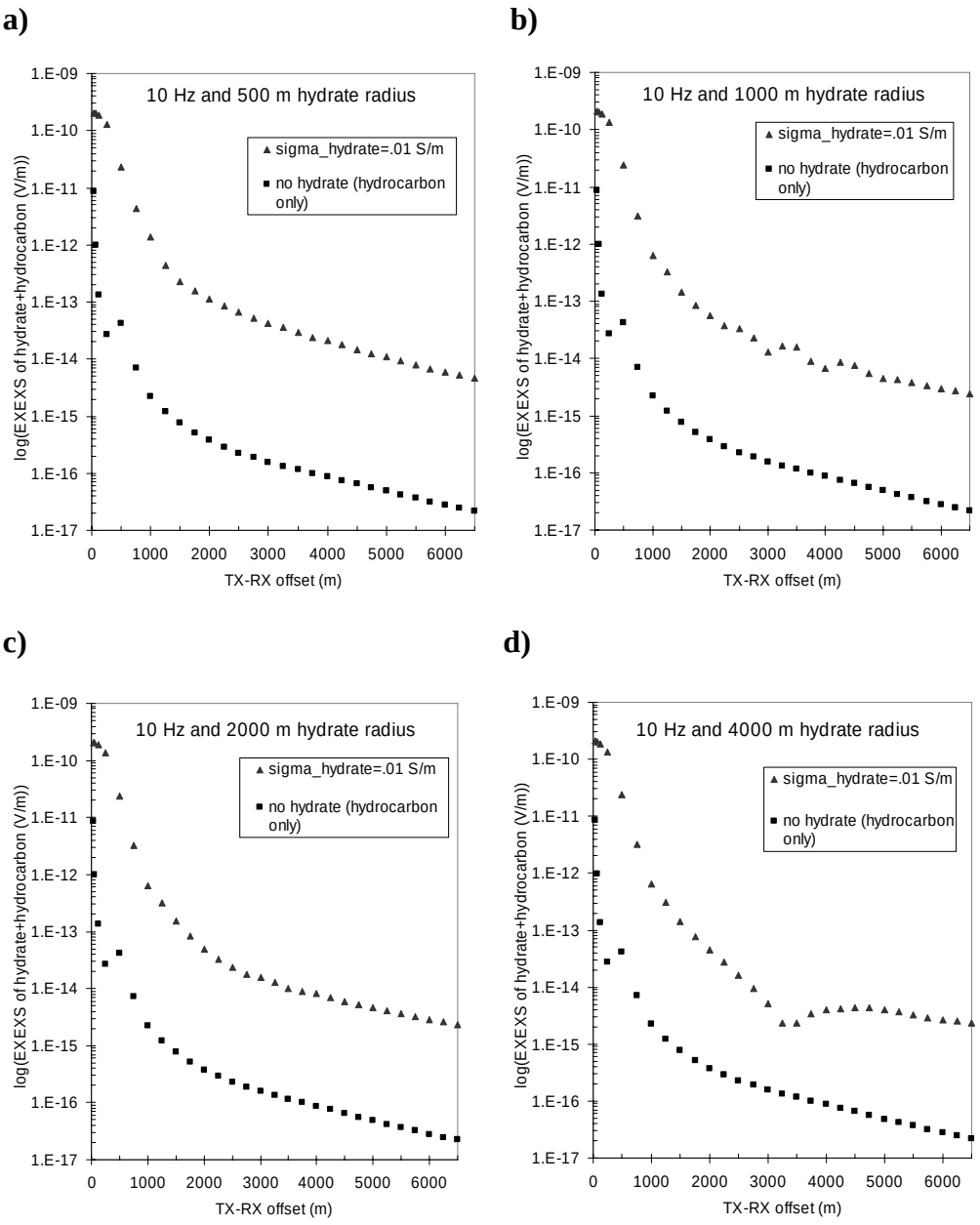

Figure 17. Gas hydrate/hydrocarbon 10 Hz intermediate radii. (a) 500 m, (b) 1000 m, (c) 2000 m, and (d) 4000 m.

With increasing radius, beginning with the 4000 m response, the cusp of the field is located near 3000 m offset for the default hydrate conductivity. This location corresponds to minimal signal domination of hydrate over hydrocarbon, though even here, the response is ten times larger than in the hydrocarbon-only model.

Referring back to Figures 11-14, as frequency is increased, a decreased EXEXS from the hydrocarbon-only model generally results. This behavior is due to the increased depth penetration at lower frequencies, which provides for larger field anomalies due to the hydrocarbon at depth (1200 m-1600 m below seafloor). Higher frequencies provide better resolution of the shallow depths, including those at which the hydrate is located (150 m-300 m below seafloor). From Figures 11-14, increasing the hydrate radii results in decreased EXEXS, particularly at large TX-RX offsets.

3.4 Hydrate Thickness

In this section, I examine the effect varying hydrate thickness has on the EXEXS response of the hydrate/hydrocarbon model, as a function of TX-RX offset, for 1 Hz, 3 Hz, and 10 Hz transmission frequencies. At each frequency, only the thickness of the hydrate is varied. Gas hydrate thicknesses studied include 50 m, 100 m, 150 m, 200 m, and 250 m. Figure 18 shows that at 1 Hz transmitter frequency when gas hydrate thickness is increased an increase in EXEXS results. A similar trend with changes in hydrate thickness can be seen at 3 Hz and 10 Hz frequencies, and the corresponding graphs will therefore not be shown. Perturbations in the EXEXS response introduced by changing the hydrate thickness in the gas hydrate/hydrocarbon model vary with offset

(with respect to EXEXS magnitude differences). Perturbations in hydrate thickness result in larger magnitude changes at near offsets relative to further offsets.

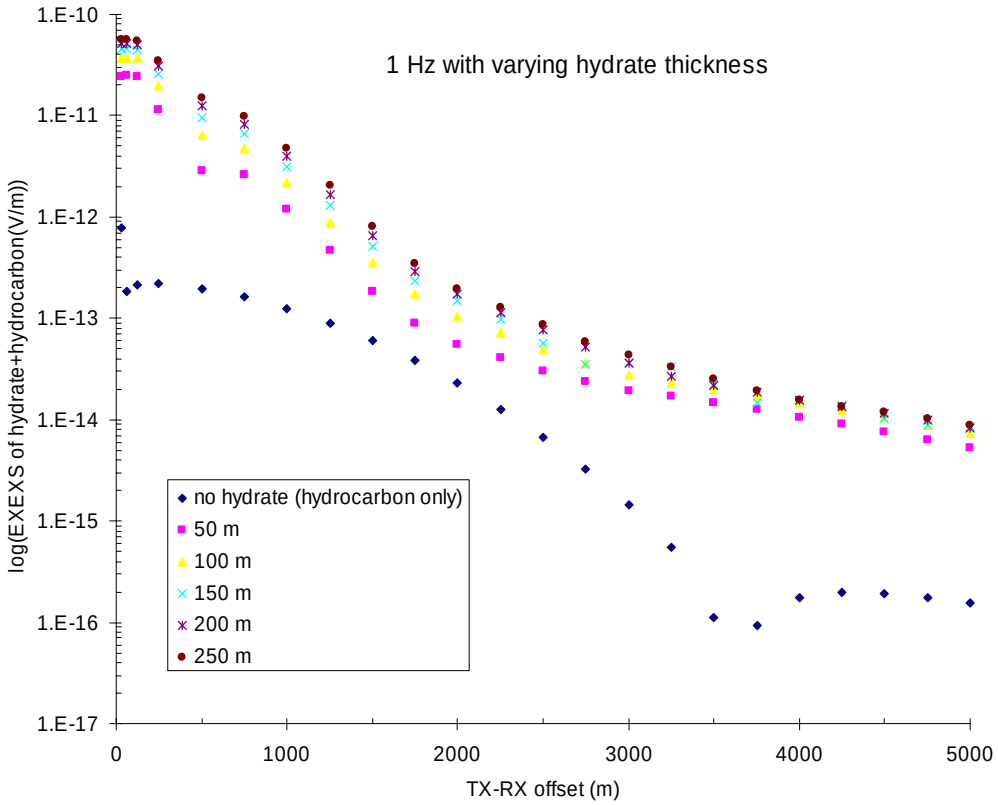

Figure 18. Varying hydrate thickness. EXEXS response of gas hydrate/hydrocarbon model at 1 Hz, with varying hydrate thickness.

Figure 19a shows the results at 1 Hz and 50 m hydrate thickness. As the conductivity of the hydrate formation is increased, EXEXS responses decrease in magnitude. Increase in hydrate conductivity causes the hydrate to become less anomalous with respect to the host material (conductivity 1.0 S/m). The physical basis for lower EXEXS response with increasing conductivity of the hydrate is that, surface

charge accumulation on the boundaries of the hydrate due to normally incident currents, decreases. At near-zero TX-RX offsets, in which receivers are located directly above the center of the hydrate and hydrocarbon disks, the largest EXEXS magnitudes are recorded. At the 1250-2500 m offset range, a relative low hydrate/hydrocarbon response and a relative high hydrocarbon-only response is observed. At this offset range, receiver responses are least dominated by the hydrate relative to all other offsets. In particular, on the 0.5 S/m hydrate conductivity curve, we see that at 1750 m offset receiver EXEXS response is dominated by fields due to the hydrocarbon. This means that adding the hydrate does not change the EXEXS response at 1750 m offset.

In Figure 19b, corresponding to hydrate thickness of 250 m, EXEXS magnitudes at all offsets are relatively larger than with the 50 m hydrate thickness. At offsets near hydrate edge (2000 m), EXEXS is increased five-fold in the 250 m case, relative to the 50 m case. A simplified explanation is that thicker gas hydrate results in a larger secondary field anomaly, because more vertical source current loops are inductively coupled with the sides of the hydrate (Sinha, 1999). A hydrate dominated response exists at all offsets, but like the 50 m scenario, is least dominant at 1250-2500 m offsets. Additionally, Figure 19b includes two extra hydrate conductivity curves, namely .75 S/m and .95 S/m. These values represent unrealistically low hydrate saturations, but illustrate that slight changes in conductivity affect EXEXS response curve shapes.

Figures 20a-c, shows the 1 Hz intermediate responses of 100 m, 150 m, and 200 m. Similar to the end-member responses, increased hydrate thickness results in a larger EXEXS magnitude at all offsets (curves increasingly separate as thickness is increased).

a)

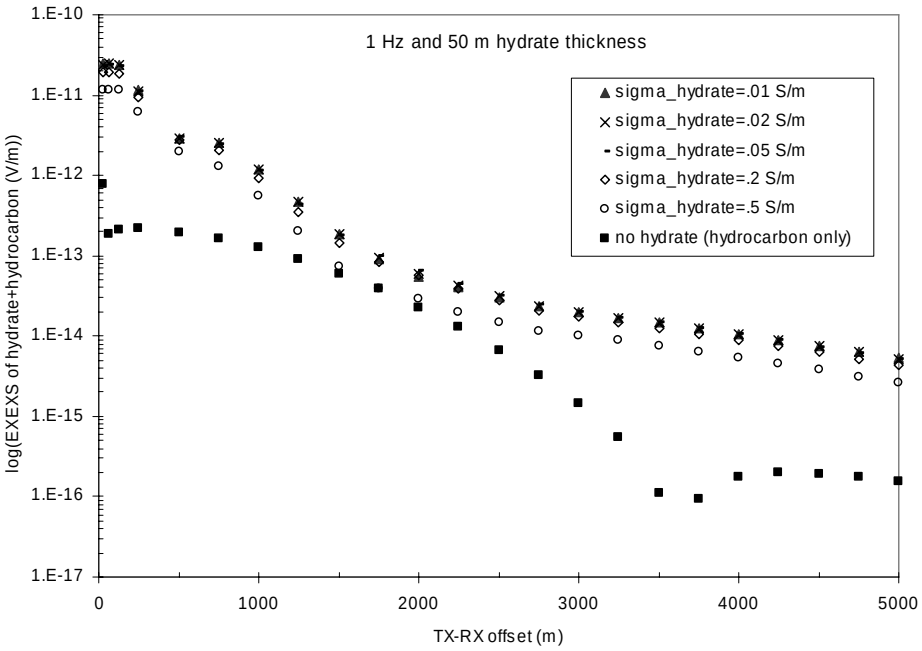

b)

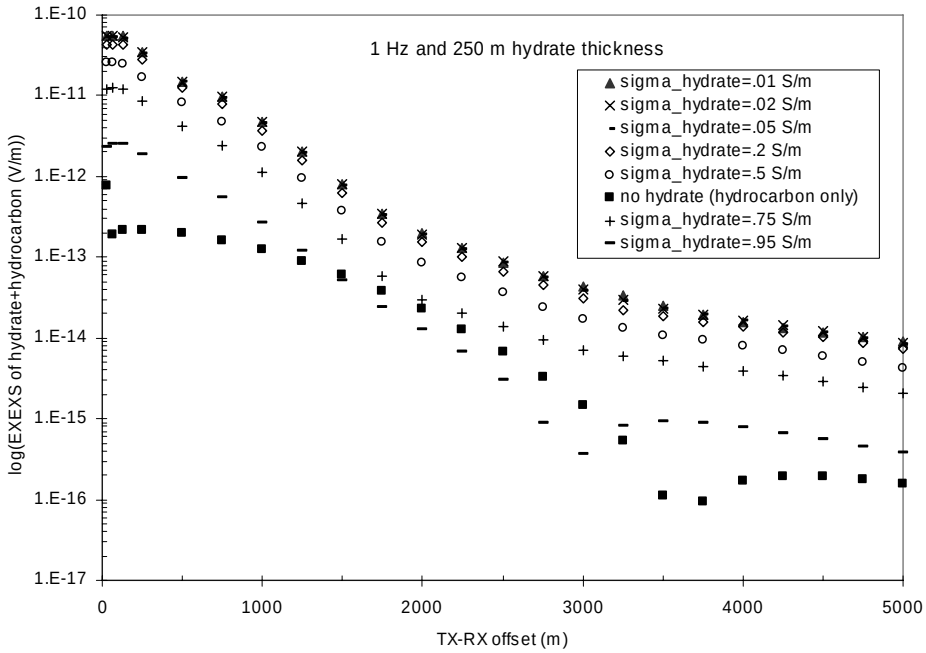

Figure 19. Gas hydrate/hydrocarbon 1 Hz endmember thicknesses. (a) 50 m hydrate thickness and (b) 250 m hydrate thickness.

a)

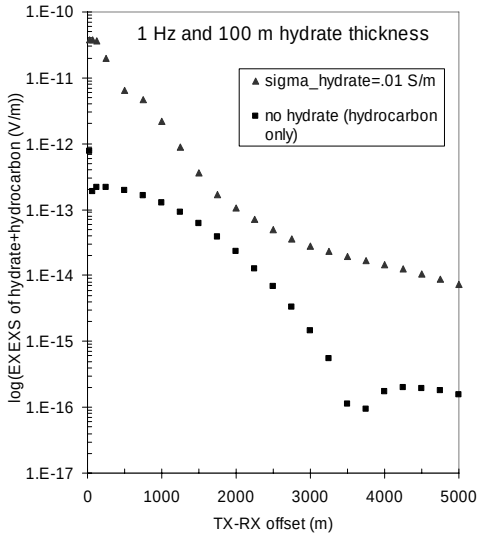

b)

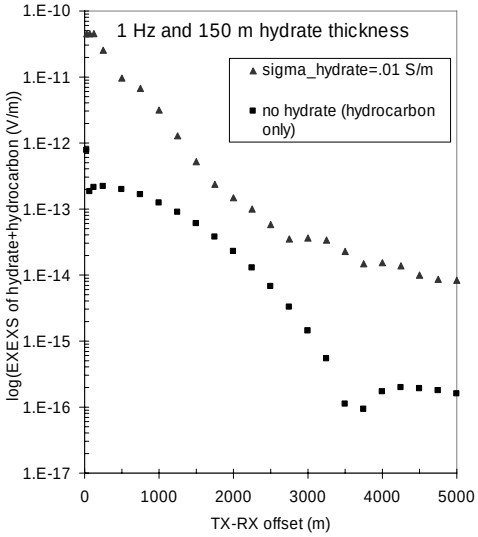

c)

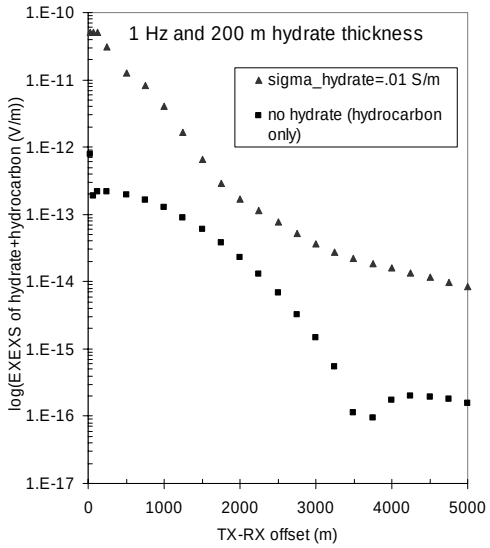

Figure 20. Gas hydrate/hydrocarbon 1 Hz intermediate thicknesses. (a) 100 m, (b) 150 m, and (c) 200 m.

From Figure 21a, it is observed that at 3 Hz and hydrate thickness of 50 m, EXEXS magnitudes are higher at near offsets (up to ~750 m), but lower at all other offsets, relative to the 1 Hz, 50 m thick case (Figure 19a). This may be partially due to increased attenuation of the electric fields at 3 Hz, since the skin depth at 3 Hz is roughly 58% smaller than the skin depth at 1 Hz. At 1500-2500 m offset we see anomalous changes with respect to hydrate conductivity. At these offsets, higher hydrate conductivities yield larger EXEXS values.

Figure 21b shows the response with hydrate thickness of 250 m at 3 Hz. EXEXS magnitudes are higher at all offsets relative to the 3 Hz, 50 m thick case. Again, EXEXS magnitudes are higher at near offsets (up to ~1000 m) but lower at higher offsets, relative to the 1 Hz, 250 m thick model.

Figures 22a-c shows the 3 Hz curves at the intermediate hydrate thicknesses. From these, and the end-member curves from Figure 21, I conclude that EXEXS responses at all offsets are hydrate-dominated, regardless of thickness. Introduction of the shallower hydrate causes responses to be 2 to 3 orders of magnitude higher than the hydrocarbon-only model.

Figure 23a shows the 10 Hz, 50 m thick responses. As in the 3 Hz model, there is a hydrate saturation anomaly present at and around 2000 m offset. At near offsets, EXEXS magnitudes are larger than the 1 Hz and 3 Hz cases, but magnitudes are lower than at 1 Hz and 3 Hz past 500 m offset. Figure 23b shows how response curves change when hydrate thickness is increased from 50 m to 250 m. Increasing hydrate thickness results in larger EXEXS values at all offsets. Figures 24a, b, and c show the

a)

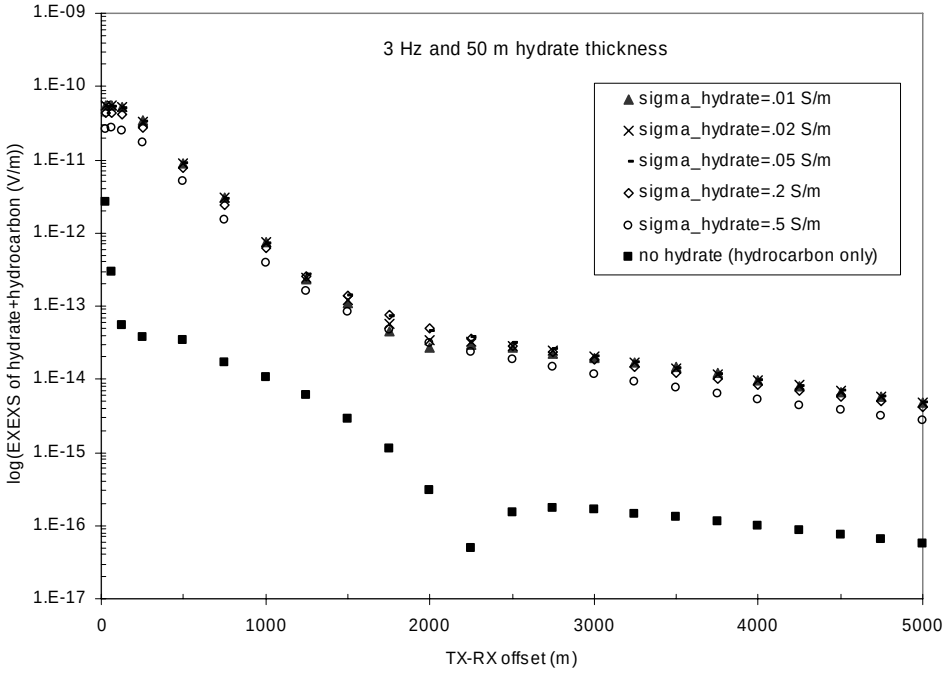

b)

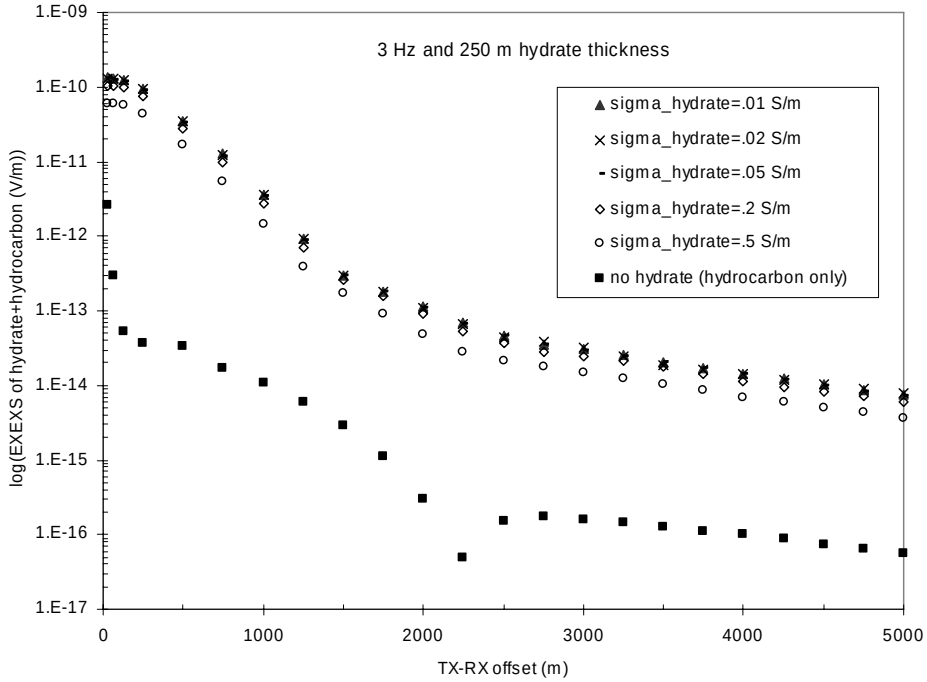

Figure 21. Gas hydrate/hydrocarbon 3 Hz endmember thicknesses. (a) 50 m hydrate thickness and (b) 250 m hydrate thickness.

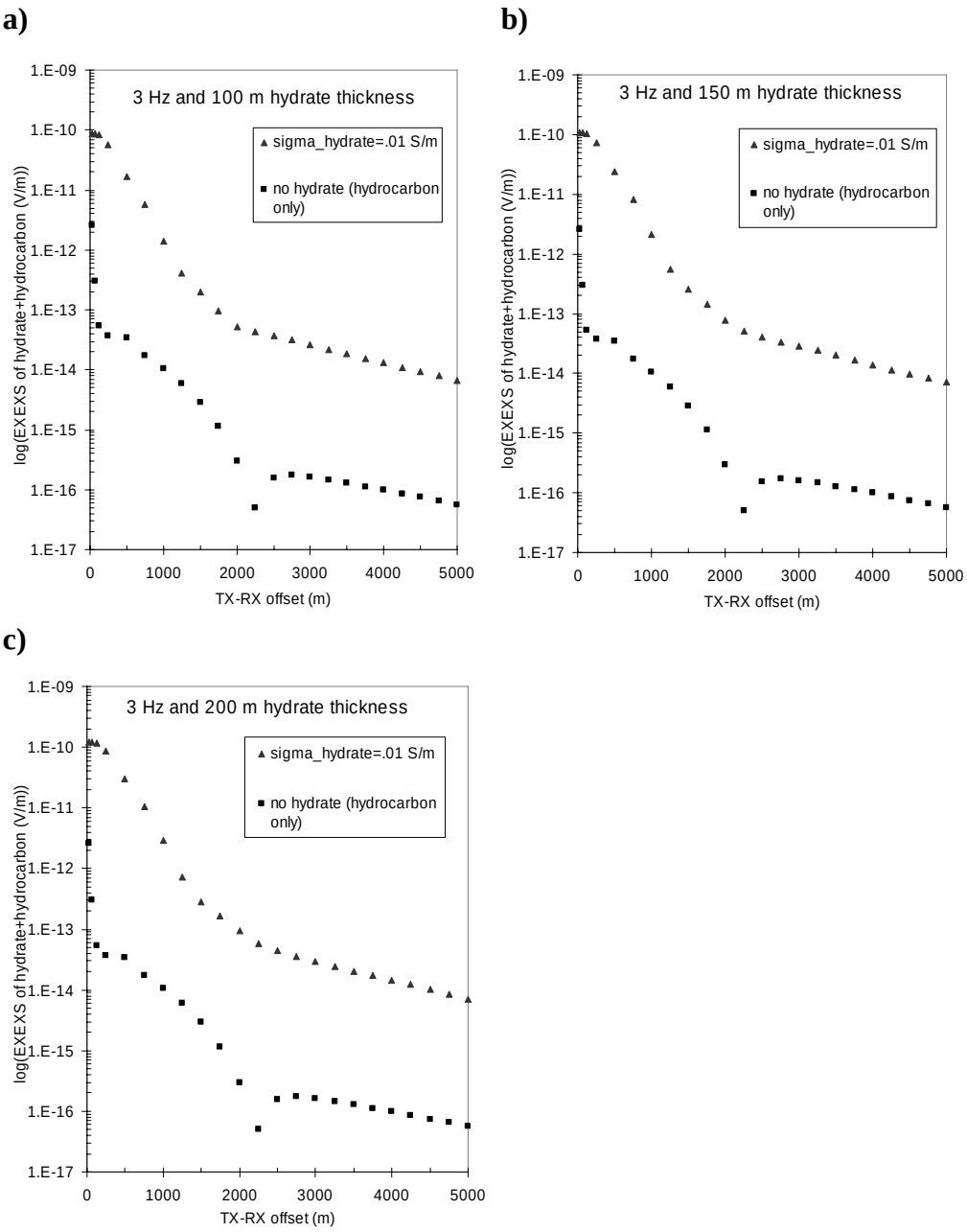

Figure 22. Gas hydrate/hydrocarbon 3 Hz intermediate thicknesses. (a) 100 m, (b) 150 m, and (c) 200 m.

a)

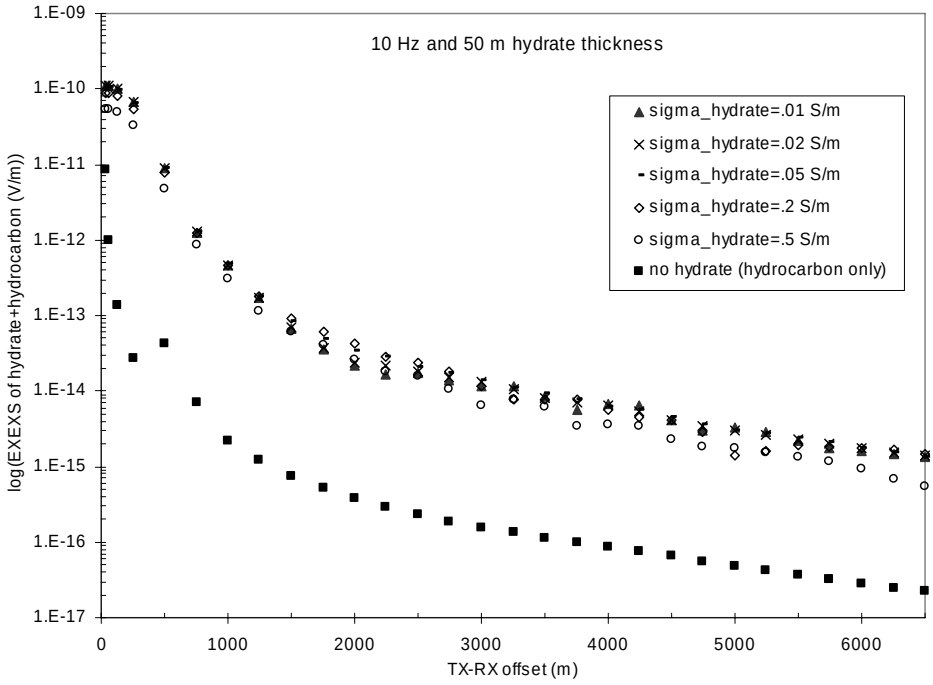

b)

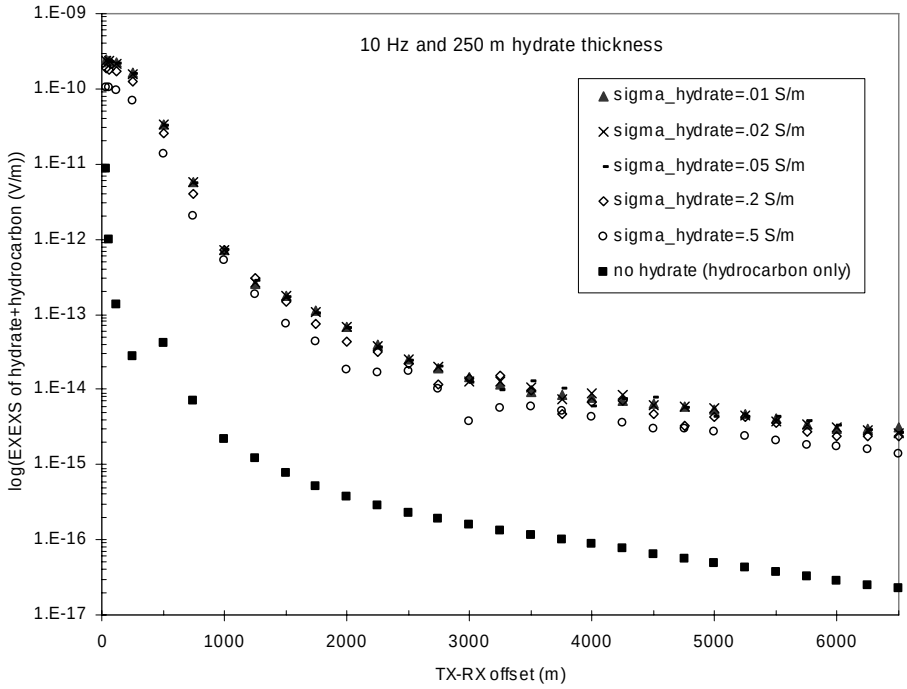

Figure 23. Gas hydrate/hydrocarbon 10 Hz endmember thicknesses. (a) 50 m hydrate thickness and (b) 250 m hydrate thickness.

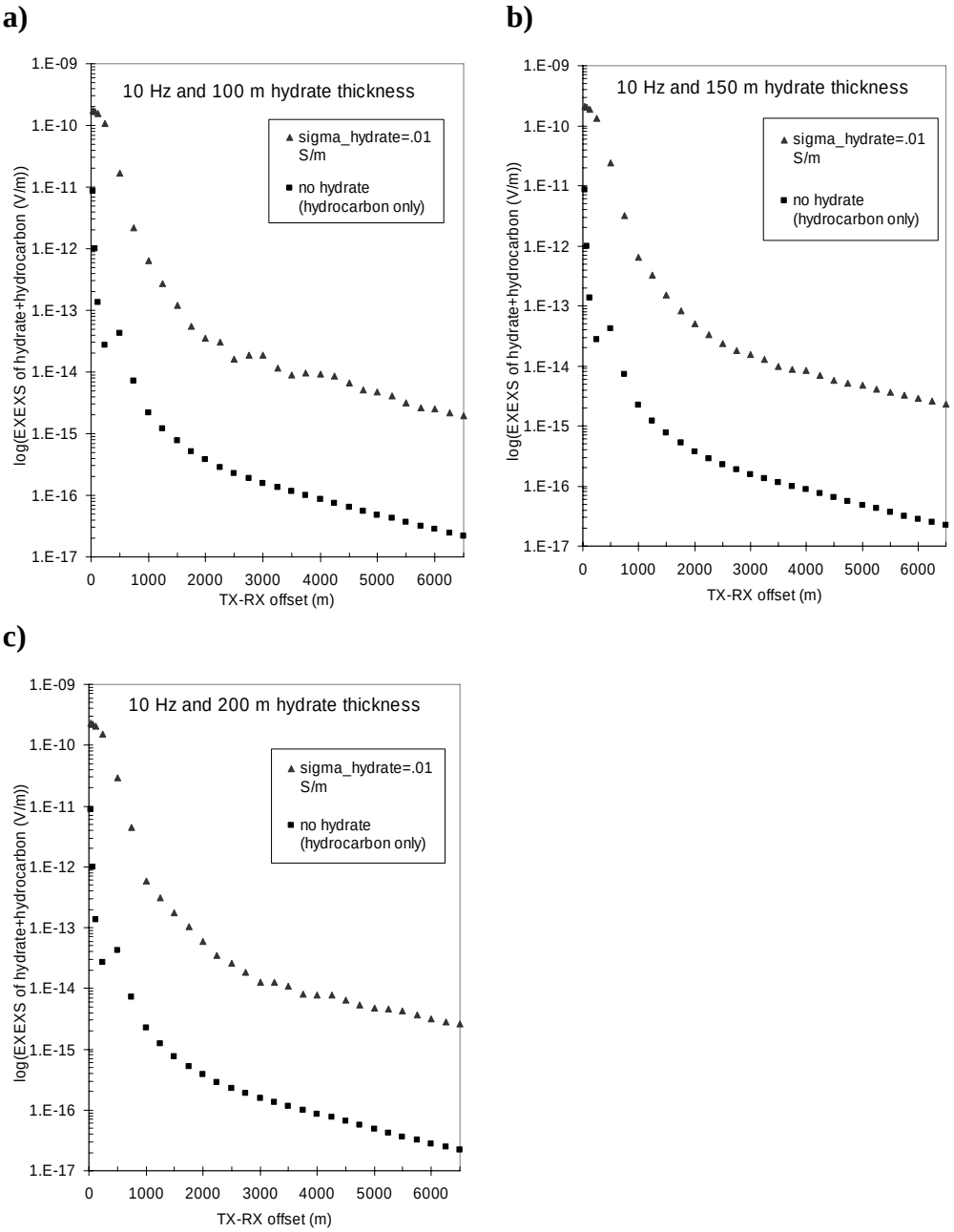

Figure 24. Gas hydrate/hydrocarbon 10 Hz intermediate thicknesses. (a) 100 m, (b) 150 m, and (c) 200 m.

intermediate hydrate thicknesses. A general increase in the magnitude of the hydrate/hydrocarbon model response is seen with increasing hydrate thickness. From Figures 23 and 24, I conclude that the hydrate EXEXS response masks the hydrocarbon EXEXS response at all offsets and all thicknesses at 10 Hz, with increased masking associated with increased hydrate thickness. The 10 Hz case is therefore no different from the 1 Hz and 3 Hz cases in that regard.

3.5 Hydrate Depth

In order to understand the effect of varying gas hydrate depth below seafloor, I examined EXEXS responses as a function of offset for the following depths to top of gas hydrate zone: 50 m, 100 m, 150 m (default), 200 m, 250 m, and 300 m.

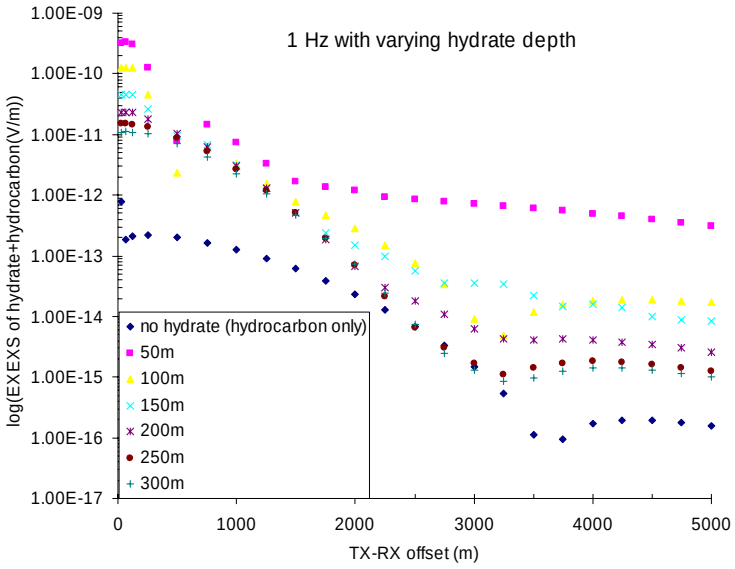

Figure 25. Varying hydrate depth. EXEXS response of gas hydrate/hydrocarbon model at 1 Hz with varying depth (50 m-300 m) to top of hydrate.

Figure 25 shows that as a general rule at 1 Hz transmitter frequency, an increase in depth to top of hydrate results in a decrease in EXEXS magnitude and therefore a decreased masking effect. Similar trends were apparent for the 3 Hz and 10 Hz cases, and the corresponding graphs at those frequencies are therefore not shown.

Figure 26a illustrates EXEXS modeled responses at 50 m hydrate depth. EXEXS magnitudes of the hydrate/hydrocarbon model are highest at very near offsets, as the secondary electric field is largest directly above the center of the disks. The EXEXS responses exhibit a sharp decrease from 250 m to 500 m offset, as these RX locations are in the cusp of the secondary field. Due to the modeled receiver spacing of 250 m, there are no receivers in place between those two offsets. However, from the shape of the responses, it is reasonable to assume that field values drop lower than $1e^{-11}$ V/m in between these receivers, corresponding to the location where the secondary electric field is mainly in the z-direction. At offsets past the cusp location, beginning at 1500 m, field falloff is much less rapid, as the horizontal contribution to electric field from the secondary response of the hydrate is increasing, (due to proximity to hydrate edge)

a)

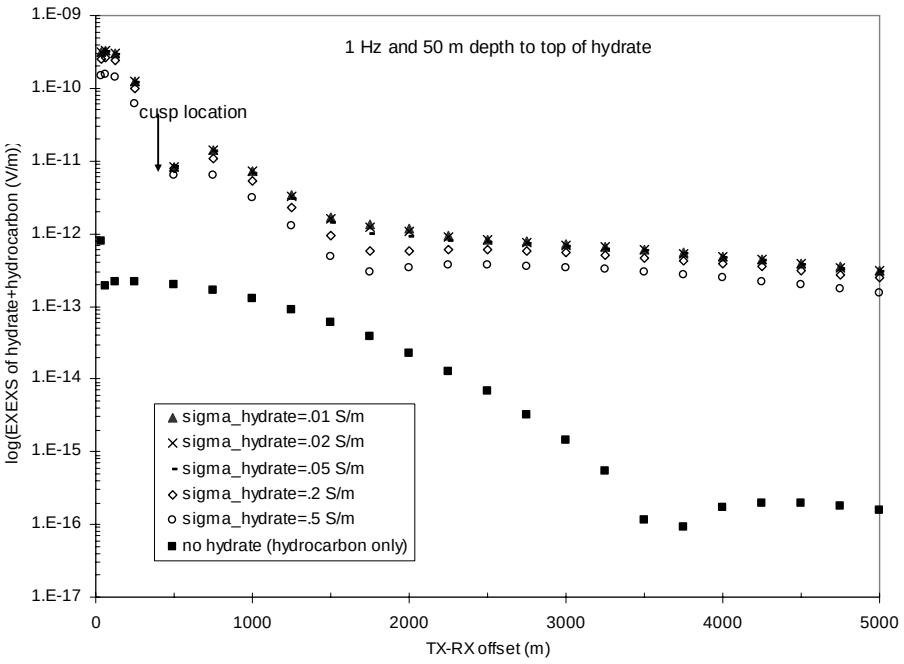

b)

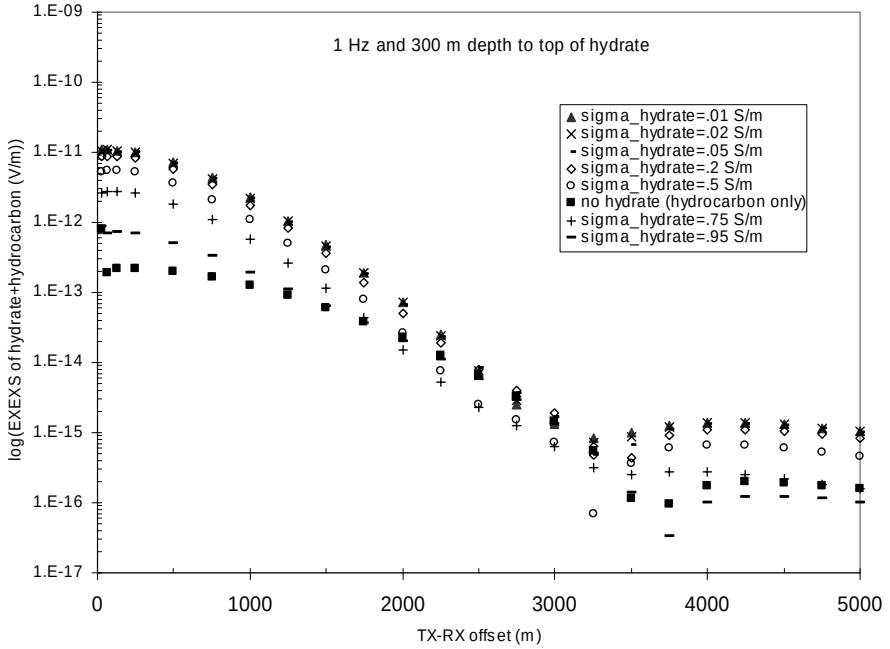

Figure 26. Gas hydrate/hydrocarbon 1 Hz endmember depths. (a) 50 m depth to top of hydrate and (b) 300 m depth to top of hydrate.

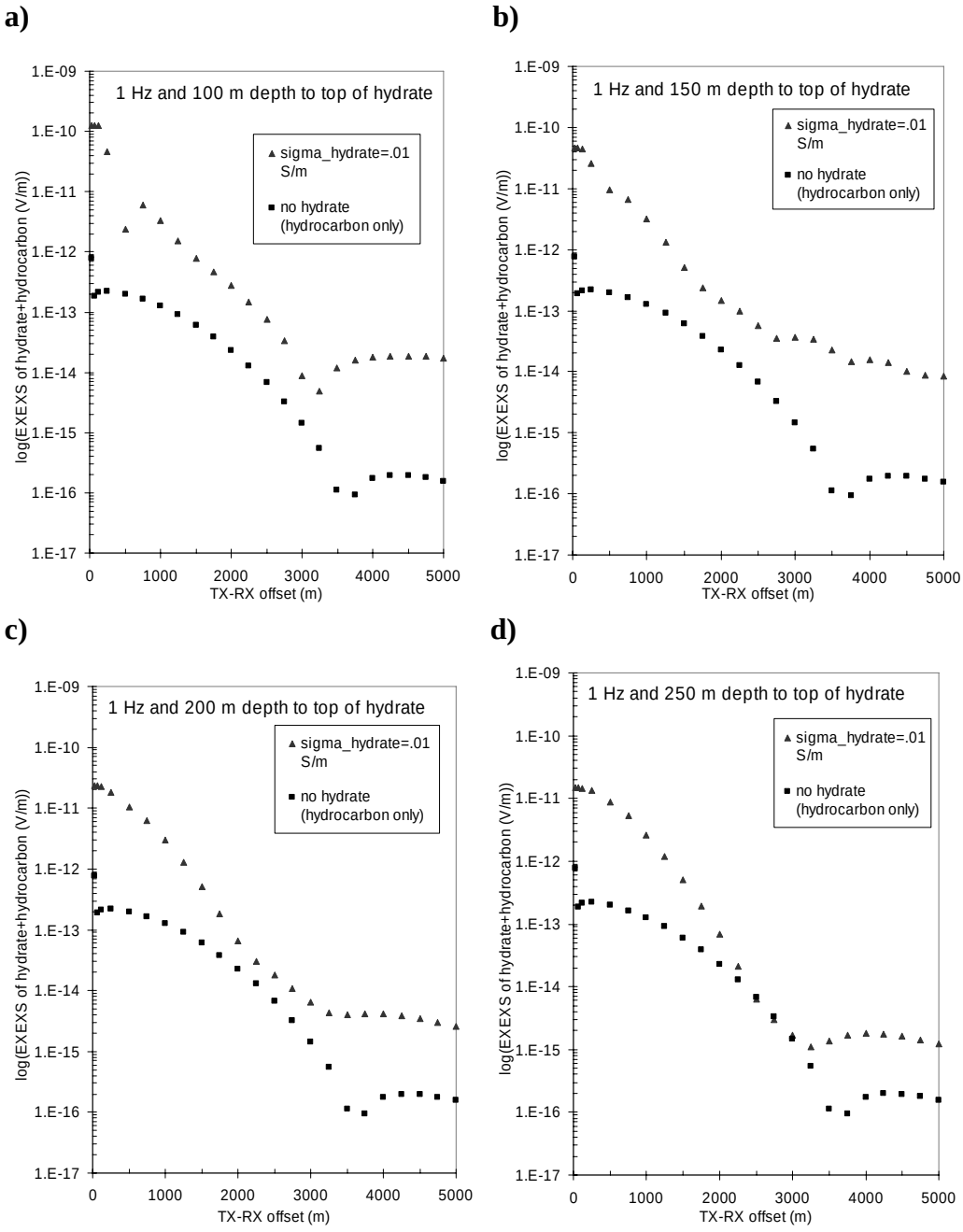

Figure 27. Gas hydrate/hydrocarbon 1 Hz intermediate depths. (a) 100 m, (b) 150 m, (c) 200 m, and (d) 250 m.

which offsets the dipole falloff and skin depth attenuation. The hydrate masking effect is prevalent at all offsets, but is at a minimum at 1750 m offset.

Figure 26b shows the 1 Hz, 300 m depth responses (with two extra hydrate conductivity variation curves; .75 S/m and .95 S/m). At near offsets, EXEXS is about one and a half orders of magnitude lower than in the 50 m depth case. Increasing the depth to top of hydrate results in a dramatic reduction in horizontal inline secondary field response. The masking effect of the hydrate on the deeper hydrocarbon is nonexistent from 2500 m to 3250 m. Receivers placed at locations in this range would be detecting a hydrocarbon response component which is greater or equal to the hydrate response component, and represents locations where "seeing" the hydrocarbon target would be optimal.

Upon examining the intermediate depth responses at 1 Hz in Figures 27a-d, we see a systematic decrease in hydrate masking effect with increase in depth to hydrate. The 250 m depth response in Figure 27d represents the depth at which we see a hydrocarbon dominated response at some TX-RX range, namely that of 2500 m-2750 m.

Relative to the 50 m depth case at 1 Hz in Figure 26a, the hydrate influenced model at 3 Hz (Figure 28a) causes larger magnitude horizontal electric fields recorded at near offsets and comparable magnitudes with the 1 Hz case at further offsets. Smaller EXEXS is recorded due to the hydrocarbon-only model at nearly all offsets. Figure 28b, the 300 m depth case, shows responses similar in those regards. This is further evidence that 3 Hz may be a better-suited frequency for probing the shallow subsurface, whereas 1 Hz is better-suited for subsurface depths similar to that of the hydrocarbon in this study.

a)

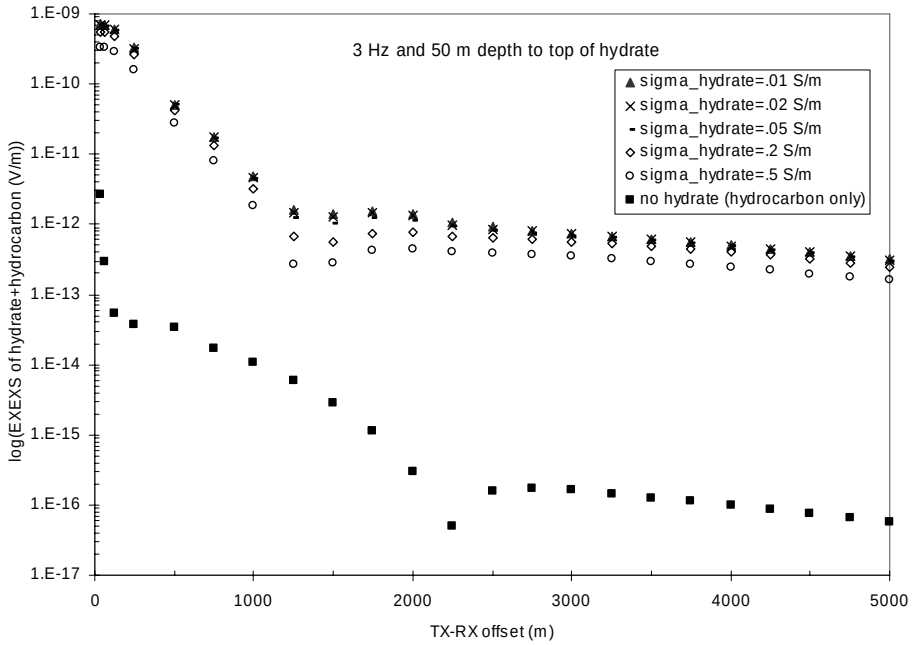

b)

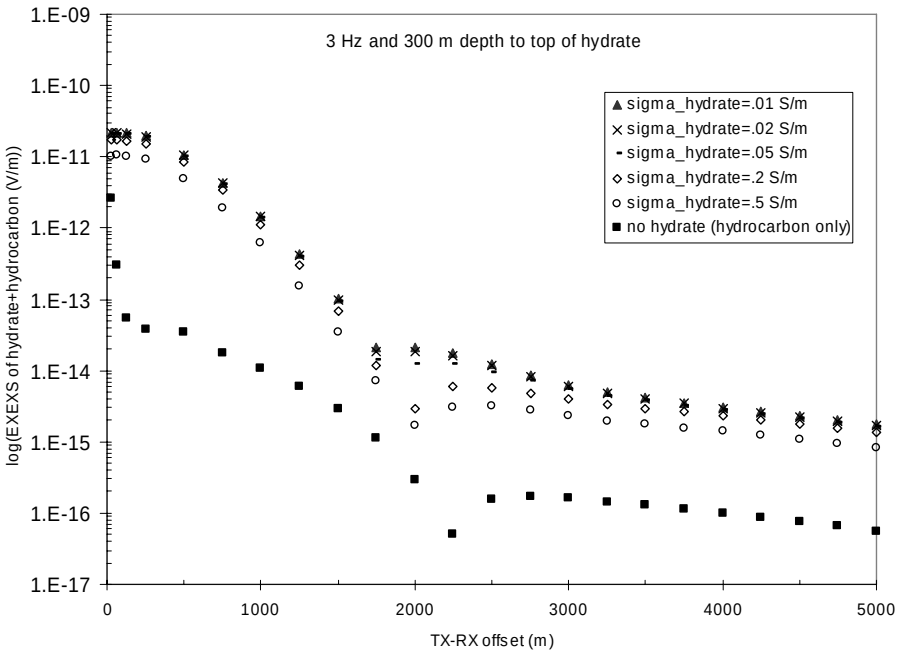

Figure 28. Gas hydrate/hydrocarbon 3 Hz endmember depths. (a) 50 m depth to top of hydrate and (b) 300 m depth to top of hydrate.

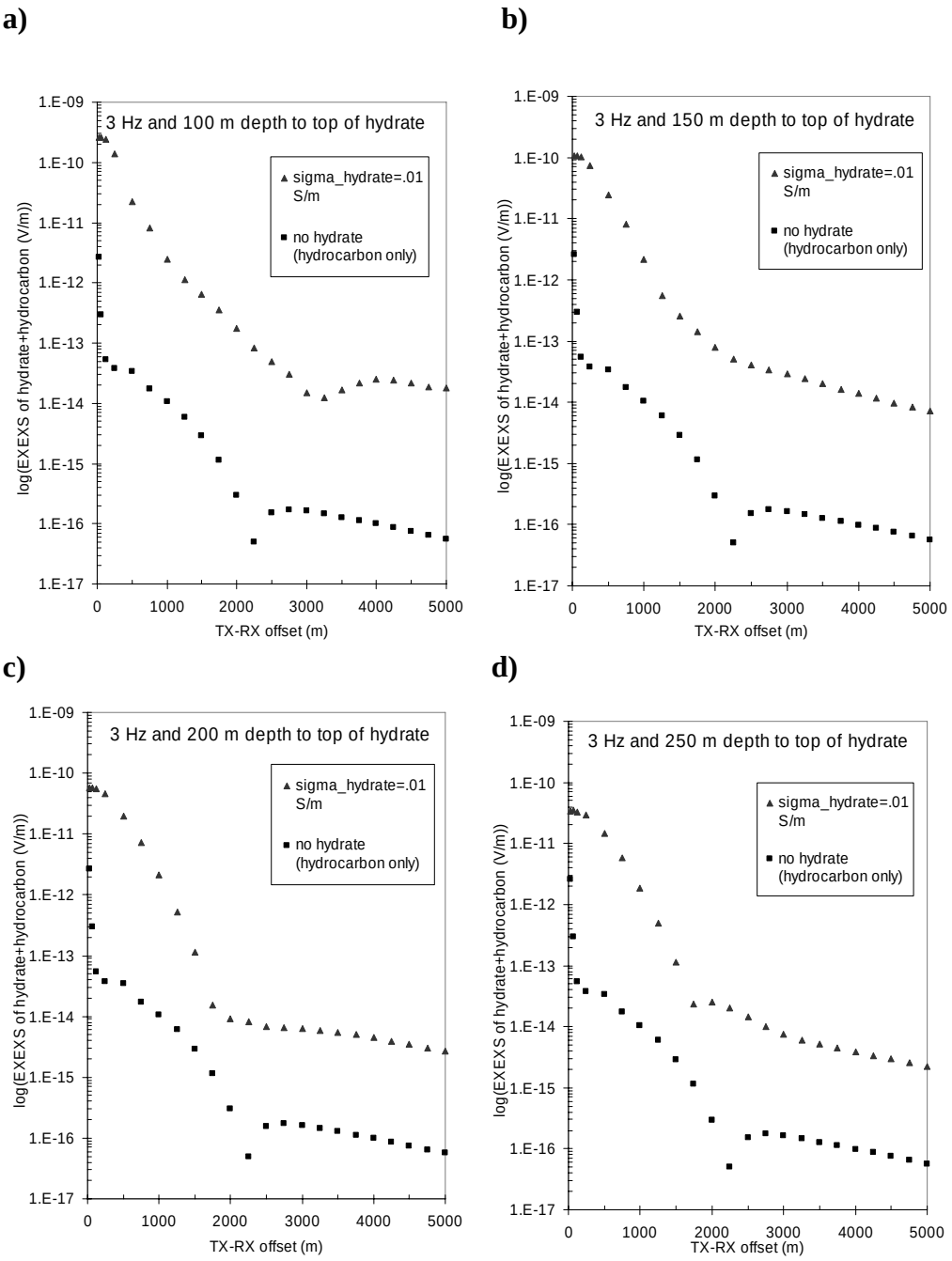

Figure 29. Gas hydrate/hydrocarbon 3 Hz intermediate depths. (a) 100 m, (b) 150 m, (c) 200 m, and (d) 250 m.

Figures 29a-d show the intermediate 3 Hz depths, illustrating a steady decrease in EXEXS as depth to top of hydrate is increased. Figures 30a and b show the extreme depth cases for 10 Hz. Again, as in the 1 Hz and 3 Hz cases, increasing the depth to the top of hydrate from 50 m to 300 m results in approximately two orders of magnitude loss in EXEXS. This is because the primary fields from the transmitter and the secondary fields from the hydrate have to travel further with increased depth to the top of hydrate, and are more attenuated. Hydrate masking exists at all offsets, but is obviously less when the hydrate is deeper.

Figure 30a shows an increase in near offset EXEXS at 10 Hz relative to the 1 Hz and 3 Hz cases at 50 m depth, but similar magnitudes at further offsets. At 10 Hz and 300 m depth of hydrate a response similar to that at 3 Hz is shown by Figures 28b and 30b, indicating that 10 Hz and 3 Hz probe subsurface depths of 300 m-450 m comparably well.

Figures 31a-d shows that the 10 Hz intermediate depth graphs display an overall decrease in horizontal electric fields at all offsets with increasing hydrate depths. Hydrate masking effect is present at all offsets, regardless of depth to top of hydrate.

a)

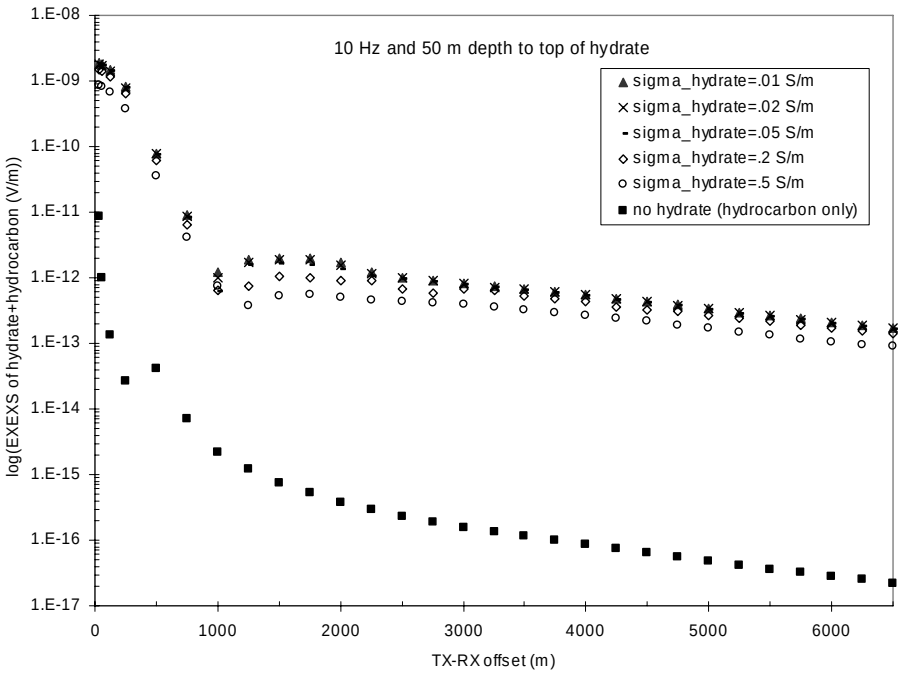

b)

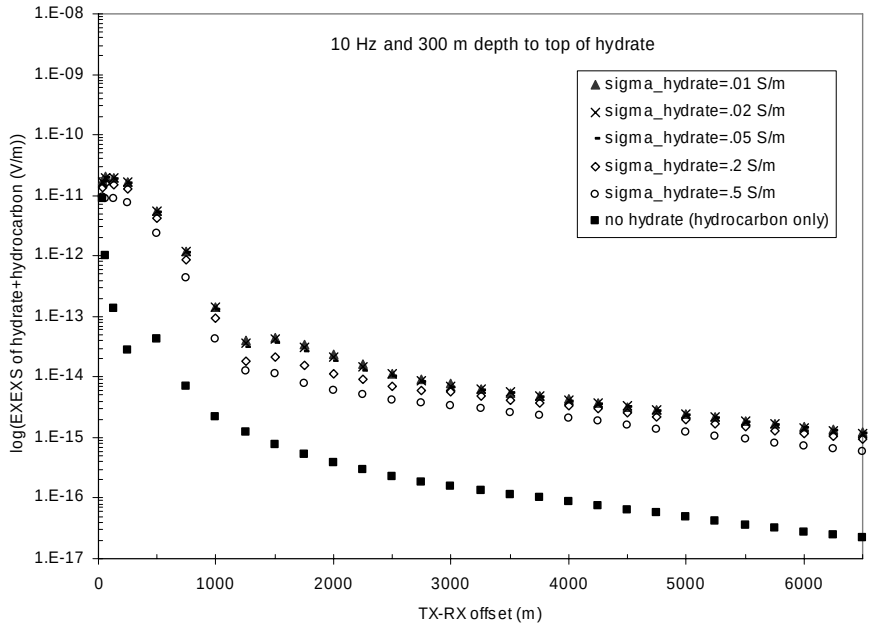

Figure 30. Gas hydrate/hydrocarbon 10 Hz endmember depths. (a) 50 m depth to top of hydrate and (b) 300 m depth to top of hydrate.

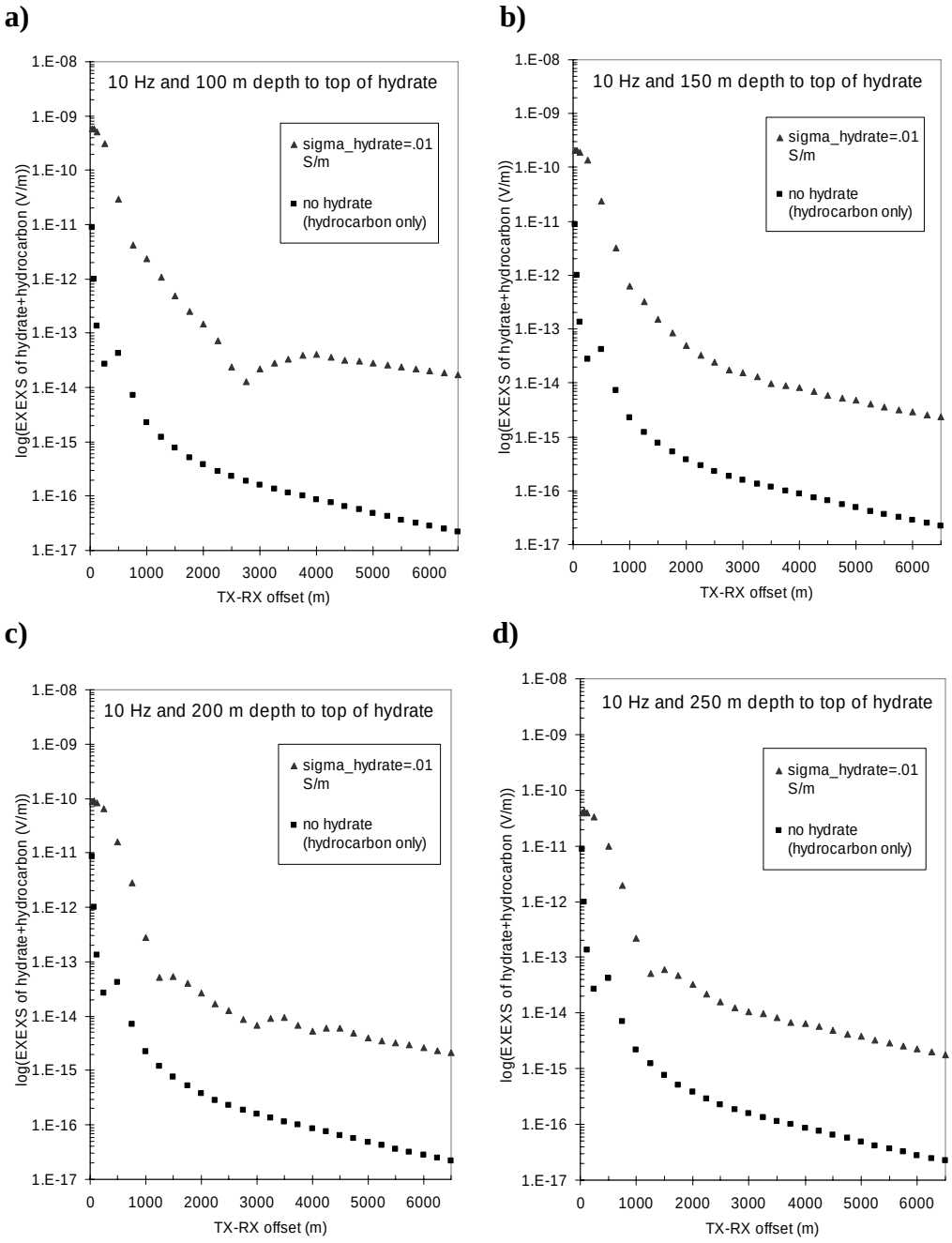

Figure 31. Gas hydrate/hydrocarbon 10 Hz intermediate depths. (a) 100 m, (b) 150 m, (c) 200 m, and (d) 250 m.

4. CONCLUSIONS

After examining the results of the new boundary conditions on a MCSEM survey model, I conclude that the new boundary condition method failed to work as hoped for shallow water depths. Incorporation of nonzero potential boundary values on the thousands of nodes located on the mesh boundary resulted in unexpected EXEXS behavior at TX-RX offsets approaching the boundary.

Results from the finite-element, forward-modeling algorithm calculations with constant boundary conditions on a simple model of a hydrocarbon reservoir in the marine subsurface show that electric field data were reliable to roughly 5000 meters of TX-RX offset for the 1 Hz and 3 Hz cases, and to 6500 meters offset for 10 Hz case.

After 3-D modeling of changing gas hydrate properties, I conclude that even a very thick and laterally extensive hydrocarbon reservoir is electromagnetically masked by a shallower gas hydrate in a conventional inline MCSEM survey, with few exceptions applying to the studied models. One of two exceptions occurs at 1 Hz transmitter frequency from 2500 m to 3000 m TX-RX offset when depth to the top of the massive gas hydrate zone is greater or equal to 250 m. Another exception occurs at 1 Hz when hydrate is 50 m thick and 150 m below the seafloor, when hydrate conductivity is 0.5 S/m, and TX-RX offset is in the 1500 m-2000 m range. Receivers at these offsets would be able to successfully detect a hydrocarbon target unmasked by the shallower gas hydrate.

Of the three main hydrate parameters studied, I conclude that disk radius has the least “predictable” effect on EXEXS responses at all frequencies studied. In many cases,

increasing the gas hydrate radius resulted in a decrease of EXEXS (and reduced masking effect). In general, for 1 Hz and 3 Hz transmitter frequencies, increasing gas hydrate radii results in increased EXEXS at offsets less than 1500 m, but decreased EXEXS at further offsets. For 10 Hz transmitter frequency, increasing hydrate radii results in increased EXEXS at offsets less than 750 m, with decreased EXEXS at further offsets.

I conclude that increase in hydrate thickness results in larger EM masking effect of gas hydrate on hydrocarbon. Variation in depth to the top of hydrate had the most effect on EXEXS responses of the three parameters studied. I conclude that larger EXEXS responses and increased masking effect can be attributed to shallower hydrate.

As a general rule, reduction in hydrate saturation resulted in a reduced masking effect of hydrate on hydrocarbon. Exceptions to this rule occur for thin hydrates (i.e. 50 m thick), at TX-RX offsets near hydrate radius (2000 m), when depth to top of hydrate is 150 m and transmitter frequency used is at or above 3 Hz. Other exceptions occur for large hydrate radii (i.e. 5000 m) at TX-RX offsets past 2000 m, when hydrate thickness is 150 m, and depth to top of hydrate is 150 m below the seafloor (for all frequencies studied).

As a general rule, the hydrocarbon is better imaged (i.e. has a stronger response) at lower frequencies, with the exception of very near offsets (< 125 m), where higher frequency causes a stronger response. In the gas hydrate/hydrocarbon model, higher transmitter frequency generally results in stronger EXEXS response at near TX-RX offsets (< 750 m). At larger TX-RX offsets, frequency-dependent imaging is more

unpredictable, but higher frequencies seem to be better suited for probing the gas hydrate, particularly when hydrate radius is small (around 250 m).

I conclude that survey design when exploring for hydrocarbons (deeper than the depths at which gas hydrates typically are found), may be improved by using lower transmitter frequency (e.g. 1 Hz). I also conclude that when using 1 Hz transmitter frequency, the hydrocarbon will appear minimally masked by the gas hydrate at TX-RX offsets beginning at 1500 m (for the cases studied), and extending to 2500 m (or beyond, in the case of deeper gas hydrates).

These findings can potentially help with risk reduction for those in the oil and gas industry performing conventional inline MCSEM surveys in regions where gas hydrate may exist. High electric field anomalies recorded at receivers when prospecting for hydrocarbons, may in fact be due to a gas hydrate saturated layer and not to a deeper hydrocarbon. It is hoped that, with this in mind, those in industry will pay close attention to survey design and interpretation (which can be improved through additional forward modeling and subsequent inversion with constraints applied from seismic, well log data, etc…), so as to optimize potential for exploration success and minimize risk.

REFERENCES

Badea, E., M. Everett, G. Newman, and O. Biro, 2001, Finite-element analysis of controlled-source electromagnetic induction using Coulomb-gauged potentials: Geophysics, **66**, 786-799.

Chave, A.D., and C.S. Cox, 1982, Controlled electromagnetic sources for measuring electrical conductivity beneath the oceans, 1, Forward problem and modeling study: Journal of Geophysical Research, **87**, 5327-5338.

Constable, S., and L.J. Srnka, 2007, An introduction to marine controlled-source electromagnetic methods for hydrocarbon exploration: Geophysics, **72**, WA3-WA12.

Constable, S., and C.J. Weiss, 2006, Mapping thin resistors and hydrocarbons with marine EM methods: Insights from 1D modeling: Geophysics, **71**, G43-G51.

Eidesmo, T., S. Ellingsrud, L. MacGregor, S. Constable, M.C. Sinha, S. Johansen, F.N. Kong, and H. Westerdahl, 2002, Sea Bed Logging (SBL), a new method for remote and direct identification of hydrocarbon filled layers in deepwater areas: First Break, **20.3**, 144-152.

Everett, M.E., and R.N. Edwards, 1993, Transient marine electromagnetics: The 2.5-D forward problem: Geophysical Journal International, **113**, 545-561.

Everett, M.E., and A. Shultz, 1996, Geomagnetic induction in a heterogeneous sphere: Azimuthally symmetric test computations and the response of an undulating 660-km discontinuity: Journal of Geophysical Research, **101**, 2765-2783.

Filloux, J.H., 1983, Seafloor magnetotelluric soundings in the Mariana island arc area, *in* D.E. Hayes, ed., Tectonic and geologic evolution of southeast Asian seas and islands Part 2: American Geophysical Union, Geophysical Monograph **27**, 255-265.

Freund, R.W., G.H. Golub, N.M. Nachtigal, 1992, Iterative solutions of linear systems: *in* A. Iserles, ed., Acta Numerica: Cambridge University Press, 57-100.

Hardage, B.A., and H.H. Roberts, 2006, Gas hydrate in the Gulf of Mexico: What and where is the seismic target?: The Leading Edge, **25**, 566-571.

Hardage, B.A., R. Remington, and H.H. Roberts, 2006, Gas hydrate-a source of shallow water flow?: The Leading Edge, **25**, 634-635.

Hato, M., T. Matsuoka, T. Inamori, and T. Saeki, 2006, Detection of methane-hydrate-bearing zones using seismic attributes analysis: The Leading Edge, **25**, 607-609.

Hoversten, G., S. Constable, and H. Morrison, 2000, Marine magnetotellurics for base-of-salt mapping: Gulf of Mexico field test at the Gemini structure: Geophysics, **65**, 1476-1488.

Hyndman, R.D., and E.E. Davis, 1992, A mechanism for the formation of methane hydrate and seafloor bottom simulation reflectors by vertical fluid expulsion: Journal of Geophysical Research, **97**, 7025-7041.

King, J., 2004, Using a 3D finite element forward modeling code to analyze resistive structures with controlled-source electromagnetics in a marine environment: M.S. Thesis, Texas A&M University.

Lau, R., 2006, A 3D finite-element modeling investigation into optimal survey parameters and direct imaging for marine controlled-source electromagnetic surveys: M.S. Thesis, Texas A&M University.

Lelievre, P.G., and D.W. Oldenburg, 2006, Magnetic forward modeling and inversion for high susceptibility: Geophysical Journal International, **166**, 76-90.

Liu, X., and P.B. Flemings, 2006, Passing gas through the hydrate stability zone at southern Hydrate Ridge, offshore Oregon: Earth and Planetary Science Letters, **241**, 211-226.

MacGregor, L., D. Andreis, J. Tomlinson, and N. Barker, 2006, Controlled-source electromagnetic imaging on the Nuggets-1 reservoir: The Leading Edge, **25**, 984-992.

Moser, J., M. Poupon, H.J. Meyer, C. Wojcik, M. Rosenquist, A. Adejonwo, and D. Smit, 2006, Integration of electromagnetic and seismic data to assess residual gas risk in the toe-thrust belt of deepwater Niger Delta: The Leading Edge, **25**, 977-982.

Sinha, M.C., 1999, Controlled source EM sounding: Survey design considerations for hydrocarbon applications: LITHOS Science Report, **1**, 95-101.

Srnka, L., J. Carazzone, M. Ephron, and E. Eriksen, 2006, Remote reservoir resistivity mapping: The Leading Edge, **25**, 972-975.

Unsworth, M., B. Travis, and A. Chave, 1993, Electromagnetic induction by a finite electric dipole source over a 2-D Earth: Geophysics, **58**, 198-214.

Yorath, C.J., R.M. Clowes, R.D. MacDonald, C. Spencer, E.E. Davis, R.D. Hyndman, K. Rohr, J.F. Sweeney, R.G. Currie, J.F. Halpenny, and D.A. Seeman, 1987, Marine multichannel seismic reflection, gravity and magnetic profiles--Vancouver Island continental margin and Juan de Fuca Ridge: Geological Survey of Canada Open File Report, 1661.

VITA

David Dickins
Email: ddickins@geo.tamu.edu

EDUCATION

Texas A&M University, College Station, TX.
M.S. in Geophysics, August 2007.

University of Texas at Austin, Austin, TX.
B.S. in Physics, May 2005.

EXPERIENCE

August 2006- May 2007 — GRADUATE TEACHING ASSISTANT for Physical Geology Labs. Dept. of Geology and Geophysics, Texas A&M University, College Station, Texas, USA.

May 2006- August 2006 — GEOPHYSICAL INTERN for Devon Energy, Houston, TX, USA.

December 2005- January 2006 — GEOLOGICAL CONTRACTOR for Comstock Resources, Frisco, TX, USA.

May 2005- August 2005 — GEOLOGICAL INTERN for Comstock Resources, Frisco, TX, USA.